



POLITECNICO DI TORINO

DIPARTIMENTO DI INGEGNERIA MECCANICA E AEROSPAZIALE

Corso di Laurea in Ingegneria meccanica

Tesi di Laurea Magistrale

Characterization of fan blade vibration with a non-contact method

Relatori

Prof. Daniele Botto

Lt. Col. Radosław Przysowa

Candidato

Pierluigi PORCO

ANNO ACCADEMICO 2018-2019

Jeśli nie teraz, kiedy?

Acknowledgements

I would like to express my deep gratitude to Professor Radosław Przysowa and Professor Daniele Botto, my research supervisors, for their patient guidance, encouragement and useful critiques of this work.

I would also like to extend my thanks to all the staff and the technicians of the laboratory of the ITWL for their help in offering me the resources for running the program.

Special thanks should be given to Jerzy Kotkowski and Edward Rokicki, for their useful and constructive recommendations on the topics of this project I was not familiar with and Wojtek Dąbrowski, who helped me in the installation of instruments.

In addition there are my friends who supported me and provided distraction to rest my mind outside of my research.

I'm particularly grateful to Dr. Andrea Nesci, who gave me good advices on how to face some issues I haven't encountered before.

Finally, I wish to thank my mother for her constant support and encouragement throughout all my study.

Summary

The aim of this work is to characterize the vibration parameters of plastic blades installed in a wind tunnel fan by means of a non-contact method, namely BTT (Blade Tip Timing). Chapter 2 is dedicated to the description of basic theory on the vibration of blades and disks.

In Chapter 3 are presented the features of BTT system, including the working principle, a few analysis techniques, the instruments usually employed and some of the main sources of uncertainty.

Chapter 4 is a complete description of the work done by the author in ITWL and AERMEC labs, focusing on the particular system analysed and on the techniques used.

It is possible to distinguish two main activities:

- FEM modeling of the system
- BTT measurements and analysis of data

The BTT method is applied in two different configurations and the results of both are presented.

Contents

1	Introduction	8
2	Blade and disk vibrations	10
2.1	Blade modes	10
2.2	Disk modes	12
2.3	Methods for improving the response	14
3	General features of BTT systems	15
3.1	Overview of blade vibration measurement techniques	15
3.2	BTT working principle	16
3.3	Data analysis	17
3.3.1	Asynchronous response analysis methods	18
3.3.2	Synchronous response analysis methods	20
3.3.3	Single Parameter Plot	21
3.4	Major sources of uncertainty	26
3.4.1	Steady axial displacements	26
3.4.2	Non-constant speed	27
3.4.3	Torsional vibrations of the shaft	27
3.5	Sensors	28
3.5.1	Inductive sensors	28
3.5.2	Optical sensors	31
3.5.3	Circumferential positioning	36
3.5.4	Axial positioning	38
3.6	Hints on blade Tip Clearance (TC) measurements	39
3.7	Real time applications	40
4	Characterization of fan blade vibration	43
4.1	Description of the system	43
4.2	Finite element model	45

4.2.1	Geometry acquisition	45
4.2.2	Material uncertainties	48
4.2.3	Blade model	49
4.2.4	Campbell diagram of the blade	56
4.2.5	Assembly model	58
4.3	Measurement system and results	60
4.3.1	TOA extraction from raw data	60
4.3.2	One optical sensor configuration	64
	Instruments	64
	Results	70
4.3.3	Six inductive sensors configuration	74
	Instruments	74
	Position of the frame	76
	Probe positions	76
	Results	78
4.4	Experimental validation of FEM model	83
4.4.1	Frequency response measurement	83
4.4.2	Damping and elastic modulus identification	85
5	Conclusions	88
	Bibliography	89
A	MatLab code	93

Nomenclature

BTC	Blade Tip Clearance
BTT	Blade Tip Timing
CT	Computed Tomography
FRF	Frequency Response Function
HCF	High Cycle Fatigue
HPT	High Pressure Turbine
LCF	Low Cycle Fatigue
LPC	Low Pressure Compressor
SNR	Signal to Noise Ratio
TOA	Time Of Arrival

Chapter 1

Introduction

In turbomachines the most stressed parts are the blades, because they are subjected simultaneously to different loads such as centrifugal force, vibrations, high temperature (in HPT and LPT stages), icing (in LPC stages or fan), high speed impacts of foreign particles and corrosion. Each one of them contributes in some way to accelerate the degradation process of the blades, thus maximum attention has to be paid on these factors during the design phase and their effects must be monitored during the operation of the system.

Since the first rotating machines were designed, one of the most common causes of failure in blades is the phenomenon of combined fatigue due to vibrations: HCF takes place during normal operation and is characterized by high frequencies, while LCF takes places during abrupt variations of speed, which for civil applications are usually limited to ground-air-ground cycles and so is characterized by much lower frequencies.

In order to predict and extend the life of blades it is then necessary to know their stress distribution and load frequency during operation, which is not a trivial task to accomplish. The type of vibration to which the blades are subjected can be classified as follows:

- Asynchronous vibrations: their frequency is not linked to the rotational speed of the assembly
- Synchronous vibrations: their frequency is an integer multiple of the rotational speed of the rotor

One of the main sources of synchronous vibration is the excitation due to a periodic fluctuation of the pressure field seen by the rotating blade during a revolution, caused by fixed stator vanes disturbing the airflow upstream of a bladed assembly. Synchronous vibrations are also generated by unbalance of rotors and, in the case of high speed manoeuvres, also by non negligible gyroscopic moments. The integer number given by the ratio between vibration frequency and rotational speed of the rotor is called Engine Order (EO) and is

fundamental for the identification of synchronous vibrations parameters.

For what concerns asynchronous vibrations, they are usually due to aerodynamic instability phenomena such as flutter and rotating stall.

Usually asynchronous vibrations prevail at lower rotational speeds, while synchronous vibrations prevail as the speed increases.

The blade vibration parameters are analysed with different approaches depending on whether we are in the design phase or in the monitoring phase. In fact during the design phase one of the main objectives is to verify that the blades don't undergo too large displacements or instability within the speed range of operation, while during the monitoring phase the focus lies on the variation of vibration parameters such as the displacements amplitude or the natural frequencies of the blades, because the shifts of these quantities are likely related to the propagation of a crack in the blade [1] [2] [3].

The structural design process aims to obtaining the stress map of the blades in order to predict the damage to which blades are subjected to during the operation of the system. The most common approach for reaching this goal consists of making a finite element model that satisfies the requirements and then validating it by means of measurements. The process is iterative, because if the measurements do not give acceptable results it is necessary to restart from the model, correcting it properly. It's not possible to obtain directly the full stress field with the actual measuring systems, so it's necessary to derive it from the measurement of point quantities such as the strain in some spots on the blade's surface or its tip displacement. From this point of view the BTT system, which will be discussed in chapter 3 is an indirect method.

Chapter 2

Blade and disk vibrations

2.1 Blade modes

The shape of a blade is too complex to be able to study it as a simple beam, in fact blades have the following features that make their structural analysis more difficult:

- The cross section is not constant, but tapered
- The blade is twisted along the principal axis in order to avoid aerodynamic problems and increase efficiency
- The cross section has a non regular shape for aerodynamic efficiency, so the centers of mass of the sections don't lie on a straight line

The listed features imply that the flexural and torsional mode shapes are often combined. For this reason the only way to perform a structural dynamic analysis is by means of a finite element model from which is possible to extract the modal shapes. In figure 2.1 there are some examples. The dashed lines represent the points which do not exhibit any displacement, so they are the nodal lines. Notice that in the torsional mode there is a point at the blade tip where the displacement is zero, one issue related to this consideration will be discussed in section 3.5.4.

Rotating blades are subjected to loads which influence their dynamic behavior and the main variables which affect the values of natural frequencies are: centrifugal force, temperature and presence of cracks.

The centrifugal force causes an increase of the natural frequencies (stiffening effect) with some corresponding changes in the mode shapes. This is due to the fact that it generates a torque which is always opposite to the displacements of the vibrating blades, both for axial and circumferential displacements.

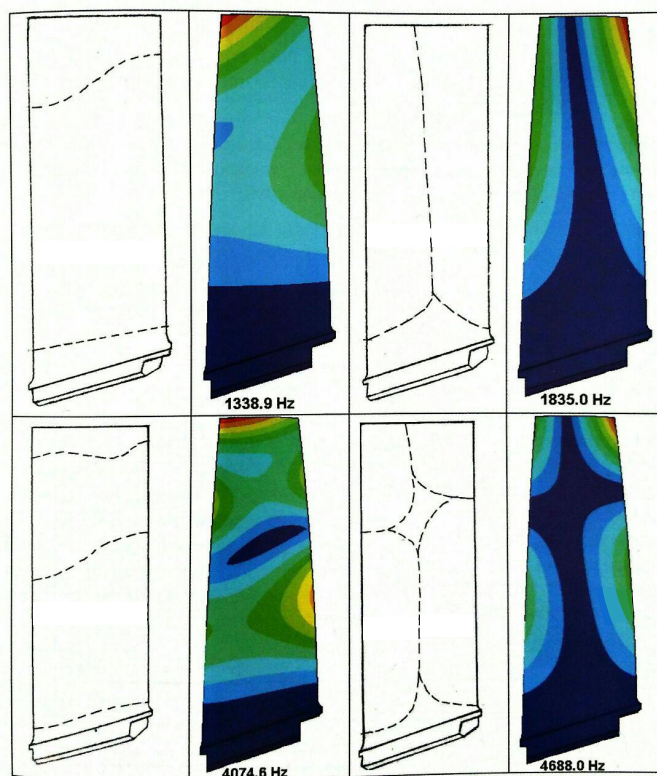


Figure 2.1: Modal displacements, from upper left to lower right: mode 2 (2nd flexural), mode 3 (1st torsional), mode 4 (3rd flexural) and mode 5 (combined mode) [3]

The temperature instead has always a de-stiffening effect as it increases.

In high pressure compressors and low pressure turbines these two effects could partially compensate each other depending on the material properties, while in low pressure compressors and high pressure turbines usually the centrifugal and thermal effect will respectively dominate, regardless of the material employed [4].

The presence of cracks has a de-stiffening effect on the dynamics of blades. This phenomenon is pretty difficult to analyze and simulate, because requires a non-linear approach due to the fact that the crack cannot be considered always open, thus a 'breathing crack' model is necessary in order to reach acceptable results [1]. In figure 2.2 it's possible to notice a decrease in the natural frequency of one blade, which was cracked on purpose for a test [3]. That's why a variation of the natural frequencies is one of the parameters that are monitored during the operation of a bladed disk. Notice that just the difference of natural frequency between blades is not necessarily symptom of damage, in fact it is most probably due to mistuning and generates the so called 'mistuning pattern'.

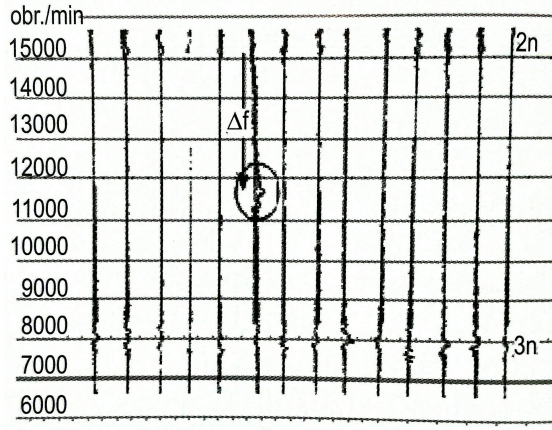


Figure 2.2: Effect of cracks on the eigenfrequencies [3]

2.2 Disk modes

Similarly to blades, also disks have eigenmodes and eigenfrequencies. The vibration of a disk is characterised by circumferential and axial sinusoidal displacements, which nodal points form concentric nodal circles and radial lines called Nodal Diameters (ND). The number of nodal diameters and circles is an indicator of the mode at which the disk is vibrating. Combinations of nodal circles and nodal diameters result in complex shapes (figure 2.3).

The disk oscillations form a circumferential sinusoidal distribution of displacements which rotates with the rotor (but not necessarily at the same speed), it is thus known generally as 'travelling wave'.

Once blades are fitted on a disk, this phenomenon continues to exist and it is even more noticeable, because generally blades are much less stiff than the disk on which they are mounted. The number of nodal diameters (and circles) increases with the speed, but there is a limit to that which depends on the number of blades [5]:

$$ND_{max} = \frac{N_{blades}}{2} \quad \text{for an even number of blades} \quad (2.1)$$

$$ND_{max} = \frac{N_{blades} - 1}{2} \quad \text{for an odd number of blades} \quad (2.2)$$

Higher numbers of nodal diameters are possible (in fact, being the system continuous, there are theoretically infinite mode shapes) but indistinguishable, that's because of the aliasing phenomenon which will be discussed in section 3.3.1 since it influences also the vibration measurements.

When combining the blades into a bladed disk, vibrations of both components must be taken into account and a coupling between the blades will exist. That's because the disk

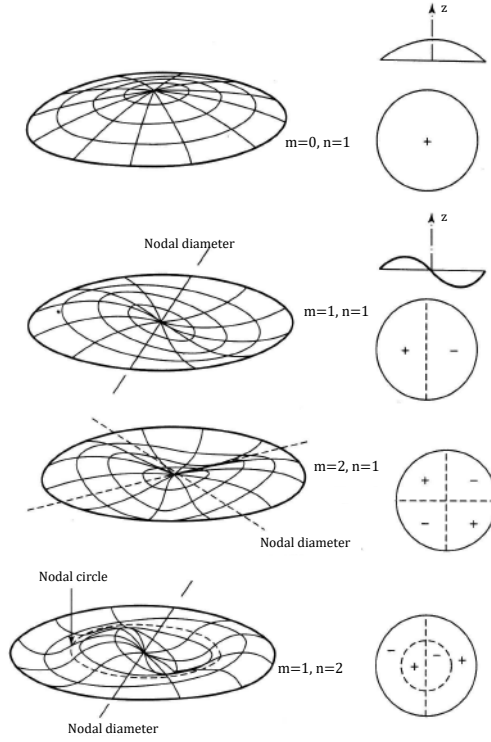


Figure 2.3: Some typical shapes assumed by a vibrating disk, m is the number of nodal diameters and n is the number of nodal circles [4]

cannot be considered perfectly rigid in most cases. In such situations the dynamic analysis of a single blade doesn't lead to accurate results which can be extended to the assembly behaviour and thus an analysis of the whole disk is necessary.

For what concerns asynchronous vibrations, the sine wave forming the circumferential amplitude distribution does not travel at the same rotational speed of the rotor, so the signal at each probe changes with time. Characterized by its frequency, the speed of a travelling wave can be converted from a static reference frame to a rotating reference frame by the following expression:

$$\omega_{rot} = \omega_{stat} - ND \cdot \Omega \quad (2.3)$$

Where ω_{rot} is the rotational speed of the travelling wave in the rotating reference frame, ω_{stat} is the frequency of the travelling wave in the stationary reference frame and ND is the number of nodal diameters.

In the case of synchronous vibrations the sine wave forming the circumferential amplitude distributions travels at the same rotational speed of the rotor but in the opposite direction

(i.e. backwards) and so appears stationary in the static fixed reference frame. This means that a stationary wave in the non rotating reference frame comes from the combination of rotating waves in the rotating reference frame. Hence, in the static reference frame, the measured phase of the targeted vibration signal at each probe does not change with time. From the mathematical point of view notice that if the vibrations are synchronous the term ω_{stat} in equation (2.3) is equal to 0 and thus in the rotating reference frame the speed of the travelling wave is naturally equal to $-ND \cdot \Omega$. In this situation there is no phase difference between the responses of the blades and the total response is one standing wave in the stationary reference frame.

2.3 Methods for improving the response

Blades mistuning

In order to avoid undesired phenomena such as simultaneous synchronous resonances, one possible solution is to perform the mistuning of blades. It is known that real bladed disks are all somehow mistuned because of tolerances issues, but it comes out that random mistuning could be a source of high amplitude oscillations which are even worse than the oscillations that would happen in case of tuned disks, so the mistuning is something that should be controlled and not left to chance.

From some studies it is known that with proper methods of intentional mistuning it is possible to reduce the amplitude of both vibrations due to random mistuning and vibrations related to the tuned disk [6]. This task can be accomplished in different ways, for example removing material from particular points of some blades or varying slightly the twist angle between root and tip. The modes of a mistuned system contain a contribution from many nodal diameters and therefore many modes can be excited by a single nodal diameter excitation [5].

Vanes mistuning

It is well known that asymmetric vane spacing can result in decreased levels of the excitation at specific frequencies. In the past it was shown that substantial reductions of the excitation level could be obtained by changing the circumferential disposition of the vanes by amounts less than $\pm 10\%$ of the normal spacing. The excitation level could be reduced in this way by an amount higher than 60% [?].

It seems that asymmetric vane spacing is a very effective method for controlling the blade response for variable speed engines where the axial rotor span cannot be lengthened. More recent studies found out that asymmetric vane spacing is effective for reduction of resonant amplitudes of a mistuned bladed disk if a multi-resonance phenomenon does not appear [7].

Chapter 3

General features of BTT systems

3.1 Overview of blade vibration measurement techniques

The techniques used for evaluating the vibration parameters of bladed assemblies can be classified in two types: contact methods and non-contact methods.

Contact methods

Two principal transducers are used in contact methods: strain gauges and accelerometers. The former represent the standard technique and have been used for many years, anyway both methods need to work in conjunction with a radio telemetry or slip rings for data transmission. For this reason there are design complications regarding the available space for the installation of the transducers, so they cannot be positioned on all the blades of a rotating disk. This is one of the main drawbacks of contact methods.

Furthermore in harsh conditions (e.g. high temperature) the accuracy of strain gauges decreases drastically, so in such cases they can be used only for estimating the oscillation frequency. Moreover, if the size of the transducer is not negligible with respect to the component on which it is installed, its influence on the dynamic behaviour of the component leads to inaccurate measurements.

Non-contact methods

During the years new systems for measuring blade's vibrations have been developed, mostly in order to achieve the following requirements which in the previous techniques are missing:

- Possibility to extract vibratory information for all the blades
- No influence on the dynamic behaviour of the system
- Good accuracy in harsh conditions
- The probes are stationary and thus less likely to be damaged

BTT system seems able to overcome (at least partially) all these problems, that's why there is a lot of research going on regarding this technique. However there are also some drawbacks:

- The quality of results depends on the probe positioning
- Signal processing is more complicated with respect to strain gauges
- Difficulty to evaluate simultaneous resonances

Its main features are briefly presented in the following sections.

3.2 BTT working principle

BTT systems are based on the following consideration: if the blades are not vibrating, the time between two consecutive passages of a blade in front of a stationary sensor depends only on the rotor speed, while in presence of oscillations the Time Of Arrival (TOA) of each blade also depends on its vibration. BTT systems usually exploit a Once-Per-Revolution (OPR) sensor to identify the blades and to define their expected TOA, even though there are other possibilities. The difference Δt between the real and the expected TOA is then used to compute the displacement of the blade tip with respect to its non-vibrating configuration, knowing the radius of the disk and its rotational speed.

In figure 3.1 the wave represents schematically a possible signal detected by the probes, for details on real signals see section 3.5.

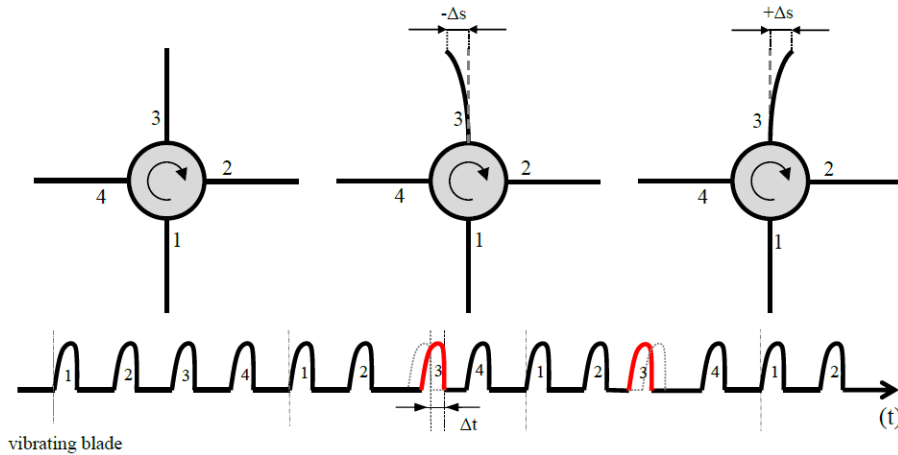


Figure 3.1: Basic principle of BTT system, Janicki et al. American Journal of Sensor Technology. 2014, 2(2), 13-19

3.3 Data analysis

In the case of a single sensor, the measured parameter is the point response sampled on consecutive rotations, this means that the acquisition is strongly aliased and an important consideration has to be made concerning the Nyquist sampling criterion: only the response components with a frequency less than half the rotation rate are defined uniquely and all other frequency components are aliases.

In practical applications more than one sensors are positioned along the circumference of the assembly, in order to get more samples per revolution for each blade and reduce the aliasing.

The determination of blade's stresses requires the response of the assembly in the rotational frame, which is obtained by sensors positioned at fixed locations in the stationary reference frame.

The Single Degree Of Freedom (SDOF) oscillator is a primary model used to describe forced blade vibrations observed by tip-timing sensors.

Furthermore different approaches for data analysis must be used depending on whether asynchronous or synchronous vibrations are considered.

Asynchronous (non-integral) response

The frequency components of the tip displacement are usually extracted by Fourier transform, which then provides amplitude and frequency of the blade tip oscillations by means of a single-blade spectrum or an all-blade spectrum.

This is perhaps the most intuitive process, however it is not the only technique employed

to obtain the desired parameters. For example it is possible to use the automated Asynchronous Averaging Built-in Matrix technique (AABM) described in [5] or even to deal with synchronous and non-synchronous vibrations together using the process developed by Russhard [8].

Synchronous (integral) response

In case of a synchronous vibration, the measured displacement samples of one blade will be the same at every revolution, as already discussed in section "Disk modes", so the frequency components of the response cannot be obtained from displacement values measured by only one sensor. Moreover in this case the maximum amplitude at resonances can only be determined from tests carried out with varying speed (acceleration or deceleration).

Static deflection information is obtained by averaging or low-pass filtering the data for each blade over some revolutions. The vibratory data that remains after subtracting the static deflection is considered as a non-integral response. The integral response is synchronized with the measurement and is hidden in the static deflection [9].

Due to tolerance issues the static deflection is not the same between different blades, resulting in the so called 'stack pattern'. A variation of the stack pattern in time can be attributed to a damage of the blades in the same way as a variation of their natural frequencies, as already discussed.

3.3.1 Asynchronous response analysis methods

The response parameters of each blade can be analysed using standard Fourier analysis techniques, and from Nyquist criterion the maximum frequency which can be evaluated is:

$$\omega_{max} = S \cdot \frac{\Omega}{2} \quad (3.1)$$

Where S is the number of probes and Ω is the rotational speed of the assembly. The maximum frequency of interest can be high enough so that in order to satisfy this condition the number of probes required can be higher than 20.

In practical applications this is not possible for two main reasons: there is no space for the installation of the probes and the quantity of data acquired would be too much in terms of computational efficiency, that's why methods based on one or two probes were developed.

Here will be briefly discussed one method involving only one measurement location.

There are two main types of analysis: single-blade spectrum and all-blade spectrum.

Single-blade spectrum

Considering that the frequency of an asynchronous response is not an integer multiple of Ω , the phase of the response samples will be different on successive rotations (figure 3.2), but as the sampling frequency approaches an integer multiple of the response frequency, the change in measured response on successive rotations will be small.

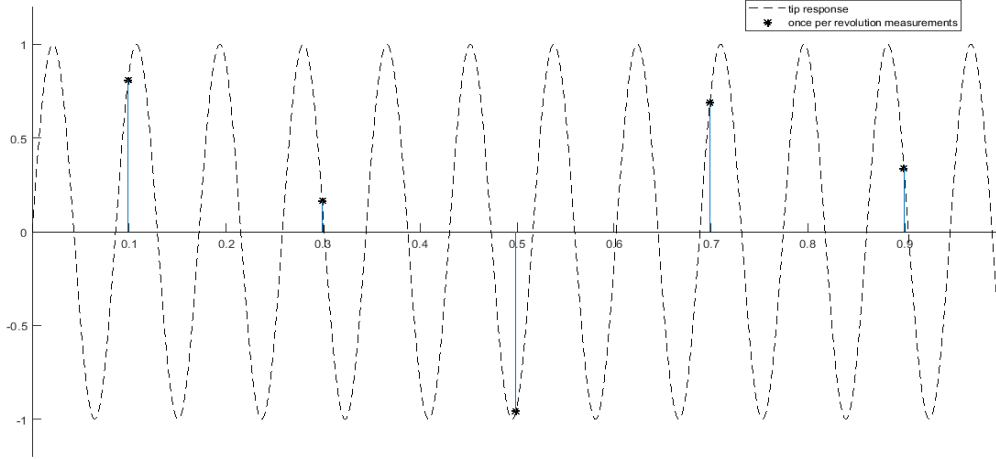


Figure 3.2: Single probe measurements

The overall response amplitude, which could contain more frequency components, is defined as the difference between the maximum and minimum response amplitudes. With only one sensor, the sampling frequency ω_s is obviously equal to Ω , so frequency components greater than $\frac{\Omega}{2}$ will be aliased in the range $0 \div \frac{\Omega}{2}$ (figure 3.3).

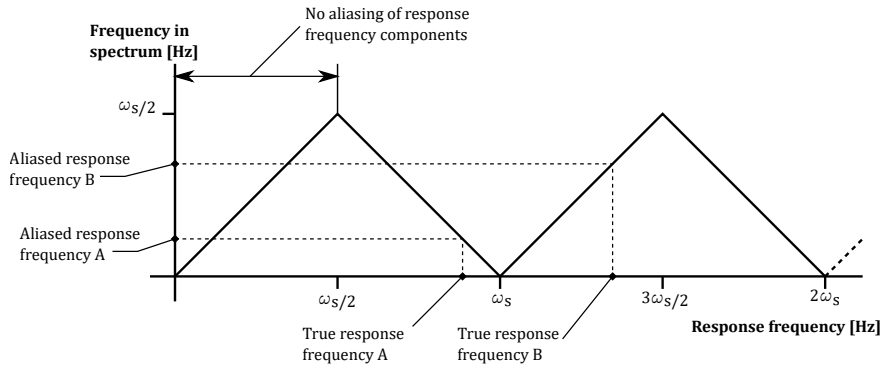


Figure 3.3: Graphical representation of aliasing

There are different techniques aiming to distinguish the true frequencies from the aliases in the individual blade spectrum, for instance the method proposed in [10] which exploits a

different variation in the response frequency $\Delta\omega_r$, due to a variation of the rotational speed $\Delta\Omega$.

All-blade spectrum

For what concerns all-blade spectrum we need to remember what has been discussed in section 'Disk modes'; if synchronous vibrations are characterized by a stationary wave in the fixed reference frame, asynchronous vibrations are characterized by a travelling wave in the fixed reference frame.

A bladed disk has a number of double modes where each pair has a certain number of nodal diameters which rotate in forward and backward direction with respect to the assembly rotation. Assuming that all blades have the same oscillation frequency, a spatial Fourier analysis of the measured response amplitude of successive blades will give the travelling wave response in the stationary reference frame.

One of the advantages of an all-blade analysis is that the sample rate is equal to the number of blades times the assembly rotation rate, so the spectrum has a wider bandwidth than single-blade spectrum. This feature usually eliminates the problems of multiple frequency aliasing for what concerns the expected resonant frequencies. Furthermore the increased spectrum bandwidth improves signal to noise ratio (SNR), allowing a better identification of spectral peaks.

Remark The standard Fourier analysis techniques assume a constant time step between samples, but of course this happens only in absence of vibrations and mistuning of the blades, thus the spectra are subjected to errors which produce some additional frequency components. These errors are usually not significant if the differences between the mean and the actual time spacings are small [11].

3.3.2 Synchronous response analysis methods

As already stated, synchronous vibrations cannot be evaluated with the same approaches used for asynchronous ones, so different techniques have been developed in the years and they can be divided in two main types: direct and indirect methods.

Direct methods

Among them, the most used are: Circumferential Fourier Fit, Global Autoregressive method and Determinant approach. The main features of direct methods are briefly condensed in the following list:

- At least four probes are needed (for Determinant approach exactly four)
- They work at a constant rotational speed of the assembly
- It is possible to determine the EO of the vibration

The amplitude of the maximum peak is not correct in all cases and the magnitude of the error varies significantly for differing probe configurations. In fact the spacing between probes can influence drastically the results obtained (see section 3.5.3).

Indirect methods

The most used are Single Parameter Plot (SPP) [12] and Two Parameter Plot (2PP) [13] [14] [15], they share the following features which are mostly in opposition to the ones related to direct methods:

- Only one (in SPP) or two (in 2PP) probes are needed
- The assembly speed must change during the measurement (acceleration or deceleration)

For what concerns the identification of the Engine Order, it is possible to achieve it with 2PP method [13] but not with SPP.

3.3.3 Single Parameter Plot

The technique was developed for the first time in 1970 by Zablotsky and Korostelev [16] and in the years has been subjected to some improvements [12]. Here follows an explanation of its working principle.

Reminding that the topic is synchronous vibrations, an appropriate synchronous excitation has to be defined along the circumferential direction:

$$F = F_0 \sin(EO \cdot \theta) \quad (3.2)$$

Where EO is the engine order of the force and can assume only integer positive values, θ is the generic angular position in the stationary reference frame with respect to an arbitrary origin. The first assumption is that the response of the blade tip can be approximated as a Single Degree Of Freedom (SDOF) system, so the measured displacement at the k-th rotation is in general:

$$x_k = X_0(\omega) \sin(\omega t_k + \phi(\omega)) \quad (3.3)$$

Where X_0 is the amplitude of the response, ϕ is the phase related to the excitation, ω is the frequency of the blade's oscillation and t_k is the TOA at rotation k. Once the origin has been fixed in the stationary reference frame, it's possible to say that at time $t = 0$ the angular position between the origin and the blade assumes a certain value γ (which of course is a constant in the present discussion). So at time t the angle between blade and origin becomes

$$\alpha = \Omega t - \gamma \quad (3.4)$$

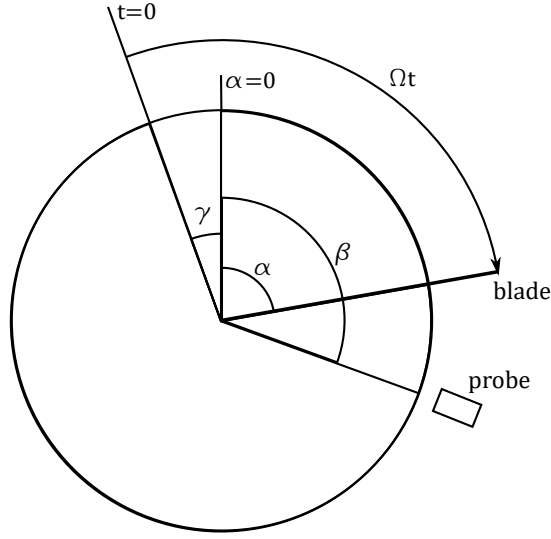


Figure 3.4: Geometrical model of the system

Notice that in equation (3.4) the vibrational term is not taken into account, but as suggested in [12] it will be considered in few steps, when computing the TOA. There is a natural relation between ω , Ω and EO , which comes from the definition of synchronous vibration:

$$\omega = EO \cdot \Omega \quad (3.5)$$

If we want to compute the force at time t on the blade we simply need to substitute θ (generic angular position) with α (blade's angular position) in equation (3.2). Then, combining equations (3.4) and (3.5) we get:

$$F = F_0 \sin(\omega t - EO\gamma) \quad (3.6)$$

In this way it's now possible to express the displacement as a continuous function of t and ω :

$$x = X_0(\omega) \sin(\omega t - EO\gamma + \phi(\omega)) \quad (3.7)$$

Let's consider now the presence of a probe at a constant angular position β with respect to the origin in the direction of rotation (figure 3.4). At time $t = 0$ the angle between the probe and the blade is $\gamma + \beta$ and in absence of vibrations the time required for the blade to pass in front of the probe after k revolutions is

$$t_k = \frac{\gamma + \beta}{\Omega} + \frac{2\pi k}{\Omega} \quad (3.8)$$

This is the approach of Zablotsky and Korostelev [16], but Heat [12] proposed an improvement which consists in considering the vibrational term when computing the TOA t_k :

$$t_k = \frac{\gamma + \beta}{\Omega} + \frac{2\pi k}{\Omega} + \frac{X_0(\omega) \sin(\omega t_k - EO\gamma + \phi(\omega))}{\Omega R} \quad (3.9)$$

Where the numerator of the last term is simply the displacement x due to vibrations at time t_k . In order to solve this equation in terms of t_k it's possible to exploit the Newton-Raphson method, because x_k depends non linearly on t_k .

Notice that up to now only analytical considerations about the synchronous vibrations have been made, but in practice with BTT method the known (measured) parameter is the TOA t_k , which is substituted in equation (3.7) in order to get the displacement.

In this work the Zablotsky- Korostelev method (3.8) is used, even though it leads to some small errors which depend on the probe position and the ratio $\frac{X_0}{R}$ [12]. This choice is due to the fact that this formulation is more immediate to understand and also this error is much smaller than other uncertainties described in section 3.4. Thus, substituting (3.8) in (3.7) we get

$$x_k = X_0(\omega) \sin \left[\omega \left(\frac{\gamma + \beta}{\Omega} + \frac{2\pi k}{\Omega} \right) - EO\gamma + \phi(\omega) \right] \quad (3.10)$$

The most relevant conclusion coming from the analysis of equation (3.10) is that the measured displacement doesn't depend on t_k but only depends on Ω , that's why in order to detect synchronous vibrations with a single sensor the only way is to change the rotational speed of the assembly.

However a speed variation introduces errors in the TOA evaluation, as will be discussed in section 3.4. For this reason there is a maximum limit to the acceleration/deceleration values to use during the measurement [12]. Typical plots of the displacement as a function of Ω are represented in figure 3.5.

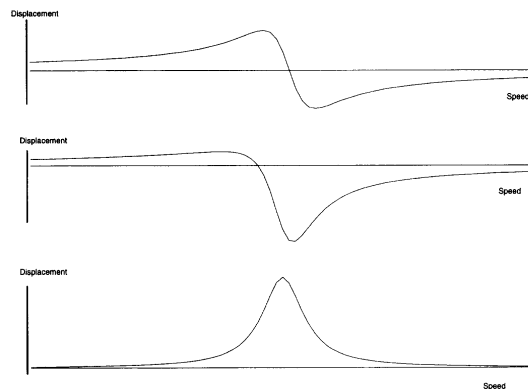


Figure 3.5: Displacement plots at different measurement positions β [12]

Notice that the probe position affects the shape of the plots, but this doesn't represent a problem because the amplitude of the displacement is given in any case by the peak-to-peak amplitude. The latter statement is valid for the Zablotsky-Korostelev formulation, but it's worth to remember that the result is not exact, because of the simplification in equation (3.8).

Once the amplitude of the vibration is known, the next parameter to be evaluated is the oscillation frequency ω . Up to now the only known value related to it is Ω , but in order to obtain ω it's necessary to know the EO of the excitation.

With a single sensor the only way to know the Engine Order related to the measured synchronous vibration is to assume it from a FEM analysis, which principal output in this case is the Campbell diagram of the blade. In fact it allows to individuate expected resonances where the Engine Order lines cross the modal lines (figure 3.6).

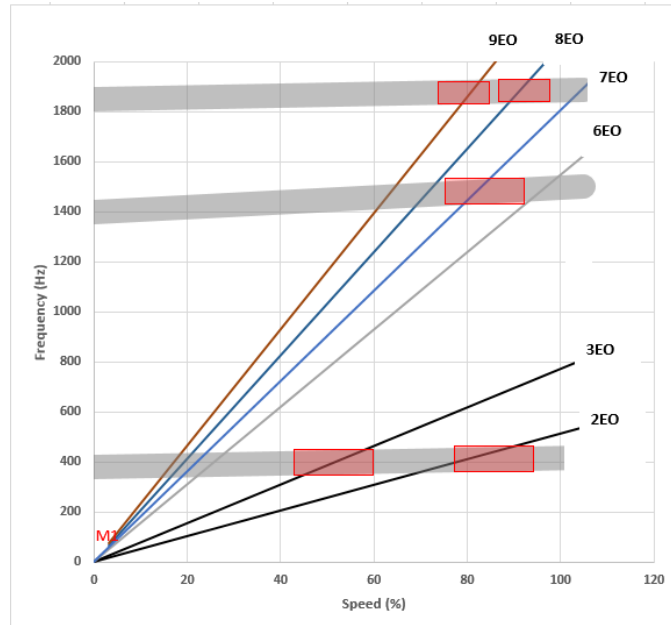


Figure 3.6: Typical Campbell diagram of a blade

Sometimes it could happen that two (or more) different EO excitations cross two (or more) different modal lines at the same rotational speed (figure 3.7, the system is considered undamped, that is why the eigenfrequencies are constant).

This phenomenon is known as "simultaneous synchronous vibration" and dealing with it is pretty complicated. That's because in this case the shape of the blade is a combination of two (or more) modes and it is very important to understand the relative influence of each one of them.

In order to solve this issue a few techniques were developed at Rolls-Royce PLC over the

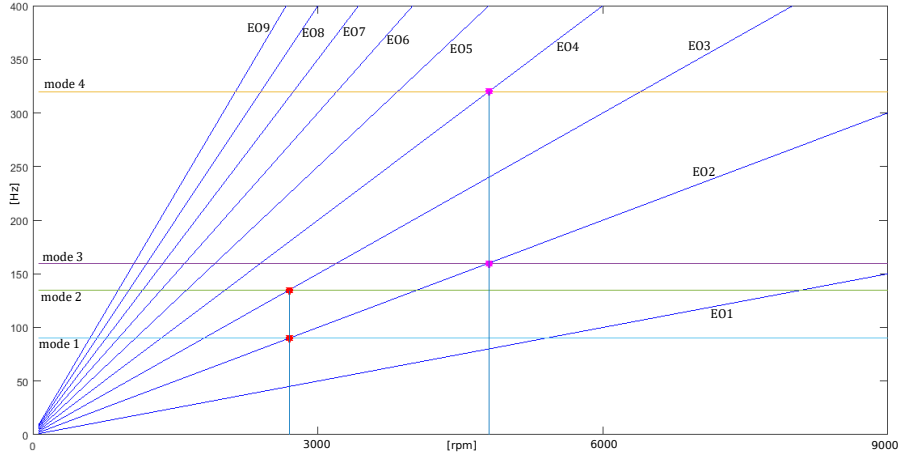


Figure 3.7: Examples of simultaneous synchronous excitations, occurring at 45 rpm (modes 1 and 2 excited) and 80 rpm (modes 3 and 4 excited). The system is considered undamped, that's why the eigenfrequencies are constant.

last 40 years but never published externally, moreover there are authors who developed other methods based on Autoregressive framework [17].

If the damping is too high, two areas of resonance in the Campbell diagram might influence each other even if they ideally occur at different assembly speeds, so the Engine Order identification might be compromised. If the damping is low enough, two consecutive areas of resonance should be sufficiently well separated to allow the identification of each one. This is very important, because the analysis of each area of resonance has to be made separately from the others.

When mistuning is not negligible, the data cannot be analysed using a single probe methodology and thus Auto-Regressive based techniques are needed. These approaches work better if data from all blades are used in order to reduce the effects of noise. However, in presence of mistuning, only data from one blade can be used and thus the AR techniques become more sensitive to noise [18].

Here the focus lies on how to combine informations coming from the measurements and from the Campbell diagram, considering low damping and absence of simultaneous synchronous resonances.

When using indirect methods, the vibration amplitude is determined by the peak-to-peak value of the measured displacement, while the Engine Order is assumed from the Campbell diagram as already explained (for SPP) or is found by means of some expressions (for 2PP) [13].

In the case of direct methods instead there are two main ways to operate [19] [20]:

- 3-parameter linear sine fitting: this method is used if the frequency of the sinusoid is

considered known (i.e from the Campbell diagram)

- 4-parameter non linear sine fitting: in this case the oscillation frequency is considered unknown (even though the Campbell diagram is available) and an iterative procedure is necessary in order to find all the coefficients

In both cases the sine wave expression is the same:

$$x[n] = A_0 \cos(2\pi f_0 t_n) + B_0 \sin(2\pi f_0 t_n) + C_0 \quad (3.11)$$

But in the first case f_0 is known, while in the second case it is unknown.

Notice that since the 4-parameter fitting is a non linear method, it needs an initial estimation of the parameters. Usually the starting value for the frequency is the one coming from the Campbell diagram (which for the 3-parameter fit is considered a fixed value).

The parameters are found in both cases by means of a least squares approach.

3.4 Major sources of uncertainty

3.4.1 Steady axial displacements

The BTT system measures only deflections in the direction of rotation, but in reality the direction of the displacement is at an arbitrary angle with respect to the tangential speed. For what concerns axial vibrations components, they can be taken into account with geometrical considerations if the blade mode shape response is known from a validated finite element model.

More complicated is the case in which axial displacements are steady, because in such case they lead to a shift of the nominal point of measurement with respect to the axial position of the probe. The displacement caused by steady movements of the blades can be of three types (figure 3.8):

- Axial shift
- Lean
- Untwist

Axial shift can be due for instance to axial elongation of the shaft caused by temperature variations or simply to the thrust that the engine provides, while lean and untwist are two conditions related mostly to centrifugal force. Moreover, lean can happen also because of a variation of the mean aerodynamic forces on the blade array.

Some techniques for taking into account these displacements have been developed ([21], [22]),

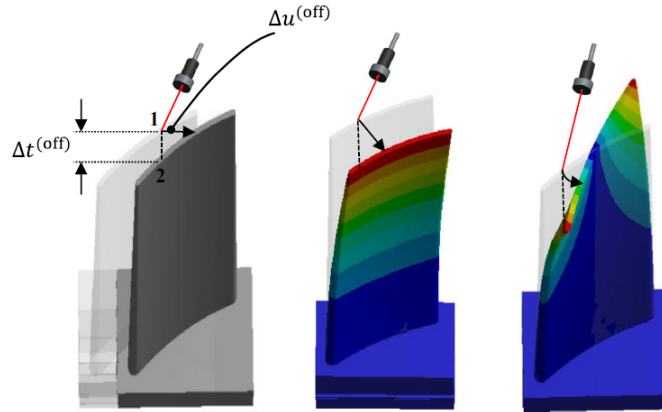


Figure 3.8: Steady axial displacements, from left to right: shift, lean, untwist

and it results that for the detection of steady untwist at least two sensors positioned at different axial locations are needed, while for detecting axial shift or lean one sensor is enough. There is another technique described in [23], where the authors suggest a system involving a particular experimental setup with digital cameras and the use of image processing in order to identify the real deformation of a working blade.

3.4.2 Non-constant speed

The expected blade arrival times are updated once per revolution and errors are introduced when the rotor velocity varies within the revolution. Current BTT algorithms assume an approximately uniform rotational speed, i.e. they are applicable for rather low accelerations/decelerations in rotor speed. In the case of engine surge, when the speed rate is very high, the procedures used to analyse the BTT data are more approximated. These errors can be reduced using multiple OPR probes to update the datum times at various points in a single revolution [11], or by modifying the algorithm [24].

3.4.3 Torsional vibrations of the shaft

Blade tip timing is based on the assumption that the rotor rotates in a steady state or, as seen in the paragraph before, with small variations of speed due to an almost constant (within each revolution) acceleration.

If torsional vibrations occur, the angular speed changes rapidly and the TOA will be different even if there's no vibration in the blades, therefore BTT data will present errors that can't be neglected.

In order to solve this problem some techniques have been developed, for example in [25] the authors propose a method which involves a further sensor near the blade roots.

However there is another issue related to torsional vibrations which depends on the position of the OPR sensor: the torsional vibration angle is as bigger as the axial distance between the bladed disk and the OPR sensor increases, reminding the well known expression:

$$\Delta\Theta = \frac{Tl}{GJ_p} \quad (3.12)$$

Where T is the dynamic torque, G is the shear modulus, J_p is the second moment of area of the shaft and l is the axial distance between the points considered.

So in order to exploit properly the correction it's necessary that the OPR sensor is positioned as close as possible to the bladed disk.

3.5 Sensors

There are different possibilities to accomplish a non-contact measurement, depending on the physical mechanisms that are exploited and on the conditions in which the sensors have to work. In fact it's possible to use magnetic, optical, capacitive or microwave transducers for the purpose [26]. Since the first two types are the most commonly used, some of their features are reported in the next paragraphs.

Whatever the technology used, an important issue related to the sensors concerns the triggering level, which is the signal value at which the TOA is recorded for each blade. This value is chosen depending on the shape of the signal, which of course depends on the signal's nature itself, as it will be explained in the next two sections.

The trigger level must be chosen in such a way that the TOA recorded is well representative of the blade's passage and is less sensitive to noise.

A common cause of mistiming in BTT is the so called spatial noise, which is a quantity calculated by dividing the peak-to-peak noise by the slope of the blade's pass pulse. In figure 3.9 the term PDF stands for Probability Density Function, it indicates the random nature of the noise which generates a random distribution in the signal and thus in the timing [27].

3.5.1 Inductive sensors

There are many types of non contact sensors which exploit magnetic phenomena, for example eddy current sensors or magnetic pickups. The shape of the signal obtained is different, so depending on this feature it comes out that some types are more suitable for BTT data acquisition than others. Eddy current sensors need an external power source, while magnetic pickups don't, that's one of the reasons why the most commonly used magnetic sensors in BTT systems are magnetic pickups (if the blade material allows their use).

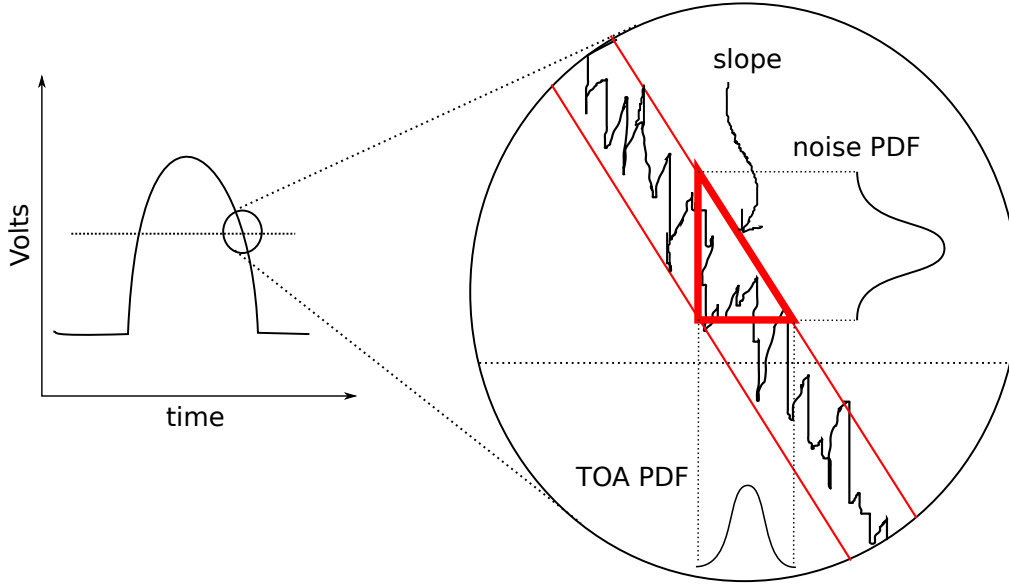


Figure 3.9: Meaning of the spatial noise

In its most basic configuration the core of the sensor is made of a permanent magnet and a coil. A variation of the magnetic flux passing through the coil is linked to the voltage between the coil's terminals, according to Lenz's law:

$$\Delta V = -\frac{d\Phi}{dt} \quad (3.13)$$

Where Φ is the magnetic flux through the coil and ΔV is the voltage between its terminals. In this case a variation of the magnetic flux coming from the permanent magnet is due to a variation of the magnetic permeability in the space nearby the sensor's extremity, caused by the passage of the blade. Inductive sensors in fact work better with ferromagnetic blades (such as steel blades) because they produce a big variation of magnetic permeability, thus resulting in a high signal-to-noise ratio. This leads to a signal which shape is similar to the one depicted in figure 3.10:

Notice that the zero-crossing of the signal occurs when the blade has maximum influence on the magnetic field generated by the permanent magnet, in fact in that moment the magnetic flux reaches its maximum value and its time derivative is zero.

Moreover, in correspondence of the zero-crossing the slope of ΔV is maximum (in modulus), so the spatial noise is minimum [27] with respect to other parts of the signal, as already explained previously. For such reason the zero crossing time is used as a trigger, specifying the sign of the slope (otherwise there would be two signals, one related to the blade and another related to the sign change between two consecutive blades).

The point with maximum slope doesn't always correspond to the zero-crossing, in fact there

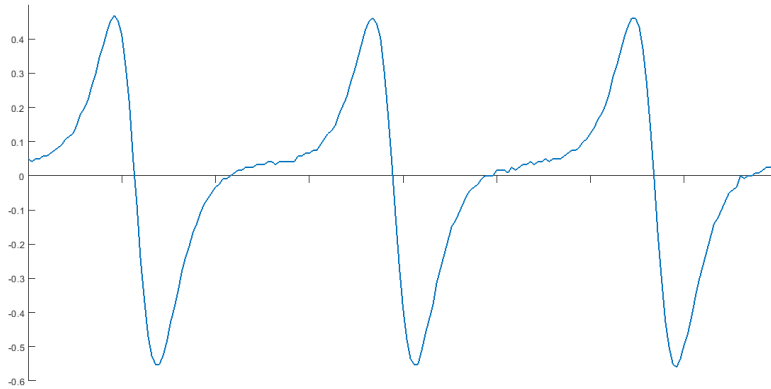


Figure 3.10: Example of typical signal recorded by magnetic pick-ups

could be an offset if the voltage at the coil's terminals is non-zero in normal conditions (without a blade nearby). One possible source of a non-zero voltage could be found in the amplifiers used in order to magnify the signal coming from the sensor for a better data acquisition.

If the blades were all exactly the same, this condition would not be a problem, but knowing that the blades are different we have to deal with the situation described in figure 3.11, where it's shown that the TOA changes in the case of a non-zero voltage.

The cause of this error is found in a different slope of the signal coming from different blades. In particular, in the figure is possible to notice that the measured time interval dt' between two consecutive blades using the zero-crossing as a trigger is different than the real time interval dt which actually corresponds to the blade's passage. This leads to a misrepresentative measurement of the tip displacement and errors in computation of stresses which can be significant.

For this type of sensors the TOA is relative to a point located at approximately half the thickness of the blade (along the circumferential direction). The slope and the width of the signal corresponding to a blade's passage depend on many variables, such as its thickness, chord angle, tip magnetization and tip clearance, these are the reasons why for different blades we have different signal shapes and it's then possible to detect for instance the mistuning due to geometrical differences between blades.

Advantages

- Possibility to work in harsh conditions with good accuracy
- Easy to manufacture, low costs
- No problems concerning tip surface irregularities

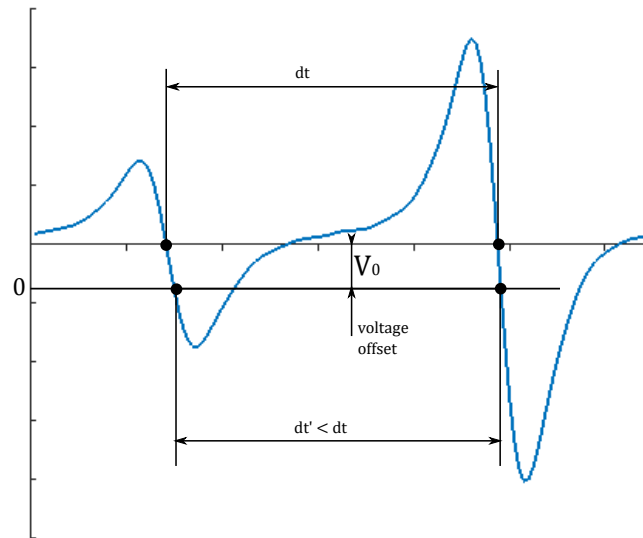


Figure 3.11: Example of signal with heavily mistuned blades and effect of non-zero base voltage

Drawbacks

- Do not work well for materials which are not ferromagnetic (such as titanium or aluminium)
- Sensitivity to magnetization of blades, leading to misrepresentative measurements
- The amplitude and slope of the signal depend on rotational speed

3.5.2 Optical sensors

The optic fiber probes used in BTT systems can be classified in two main families: un-lensed and lensed. The former have their Numerical Aperture (NA) defined by the optical fiber and must be installed close to the blade tip since the optical beam diverges, while the latter use a lens to control NA and spot size, but are more sensitive to dirt and high temperature. Furthermore the lensed probes are more expensive than the unlensed ones, in terms of initial cost and maintenance.

Most of optical sensors used for BTT are perhaps un-lensed multi-fiber, so here follows a brief description of their operation.

The probe consists generally of a bundle of several optical fibers, each a few hundredths of a millimeter in diameter. The fiber bundle is divided into two groups of fibers. One group (transmitting fibers) is exposed to a light source and thus carries light to the probe tip, where light is emitted and then reflected by the target surface.

The reflected light is picked up by the other (receiving) group of fibers, transmitted to the electronics package, and focused on a suitable photodetector whose electronics then produces a dc output related to probe-target gap (figure 3.12).

In order to optimize the sensitivity of the sensor, various configurations of the two fiber

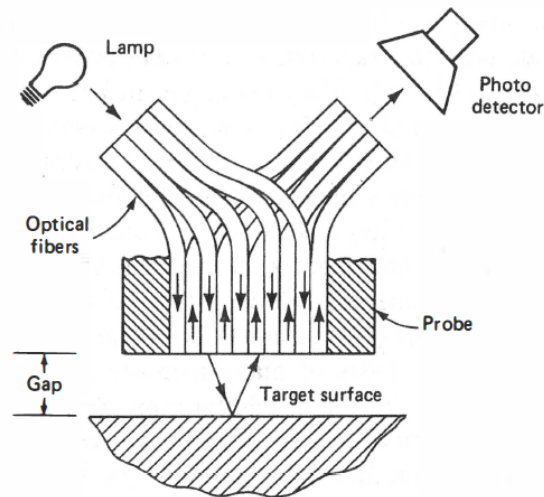


Figure 3.12: Typical configuration of a fiber-optic displacement transducer

bundles can be used. Theory shows that maximum sensitivity in the front-slope region is achieved by arranging the fibers in a precise geometric pattern in which each receiving fiber is surrounded by four transmitting fibers. This is not practical from a manufacturing viewpoint, so a random distribution, which has been found to give nearly identical results, is usually used when the sensor is employed as a proximity transducer [28].

In the case of BTT employment the optimal configuration is with few transmitting fibers in the middle surrounded by many receiving fibers, because in this way the signal slope is much more sharp.

Probes of this general type display two useful measuring ranges: front slope and back slope (figure 3.13).

At zero gap, light cannot escape from the transmitting fibers and output is zero. As the gap increases, more of the target surface is illuminated until there is a peak in the output. Motion beyond this point causes a reduction in response since both target illumination and the fraction of reflected light observed by the sensor decrease.

Similarly to inductive sensors, which sensitivity depends on the target material's magnetic properties, in the case of optical sensors the sensitivity depends on the reflectance of the target surface.

The sensor aperture represents the effective spot size that is projected onto the blade tip

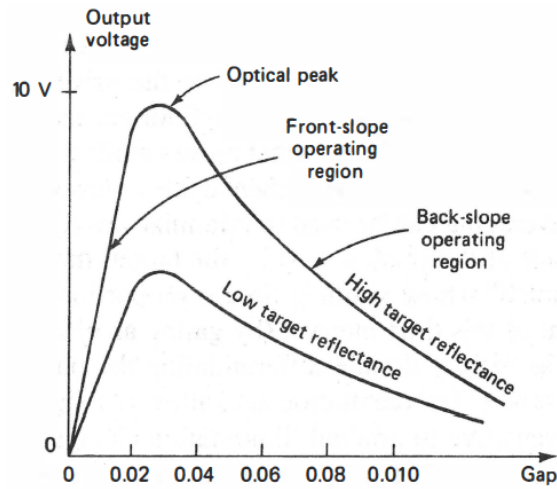


Figure 3.13: Sensitivity of fiber-optic sensor as a function of distance and reflectance of the target surface

and has to be calculated by means of the expression

$$D = 2 \cdot L \cdot \text{tg}(\theta) + d \tag{3.14}$$

Where L is the distance to the blade, θ the maximum half acceptance angle of the fiber and d is the diameter of the transmit fiber, as depicted in figure 3.14. The value of θ depends

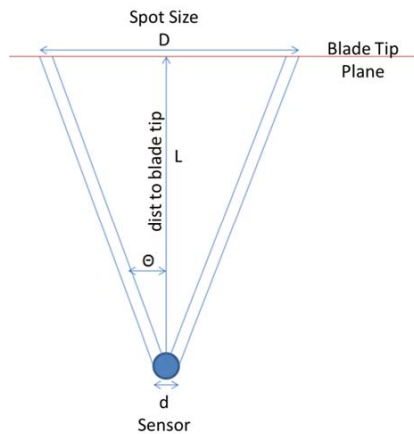


Figure 3.14: Geometrical properties of unlensed sensor system

on the already cited Numerical Aperture of the optical fiber used to transmit the light:

$$NA = n \cdot \sin(\theta) \tag{3.15}$$

Where n is the index of refraction for material outside the fiber (typically air).

It is possible to further expand the classification of optical sensors, because a variety of them is available in the market. There are in fact single fiber sensors and multi-fiber sensors which can stand temperatures up to 600 °C, air cooled sensors for temperatures up to 1100 °C and line sensors, as shown in figure 3.15. The latter are able to remove the

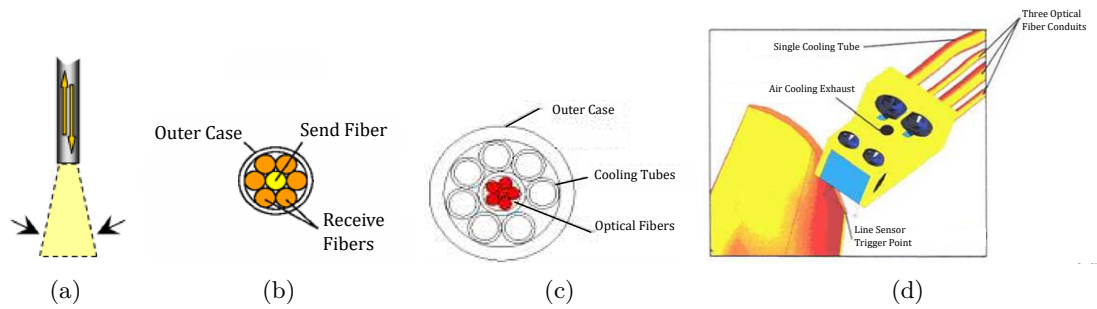


Figure 3.15: (a) Single fiber, (b) Multi-fiber uncooled, (c) Multi-fiber cooled, (d) Line, [29]

uncertainty due to axial motion because generate a signal at each passage of the leading edge regardless of the axial displacement (figure 3.16). So from this point of view they are robust, but they are also much more delicate and expensive with respect to the other types.

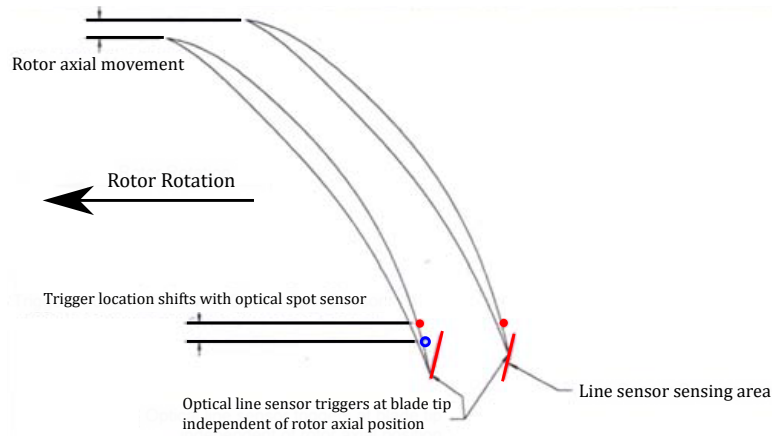


Figure 3.16: Behavior of line sensors in presence of axial steady displacement

All types of optical sensors have a similar signal shape, with a relatively high slope (in modulus) at the trigger level compared to inductive sensors (figure 3.17). This leads to a smaller spatial noise (see section 3.5) and good spatial resolution ([30]) so it's one of the advantages of optical sensors with respect to inductive ones.

Another feature of optical sensors is their high sensitivity to blade tip surface, in fact from

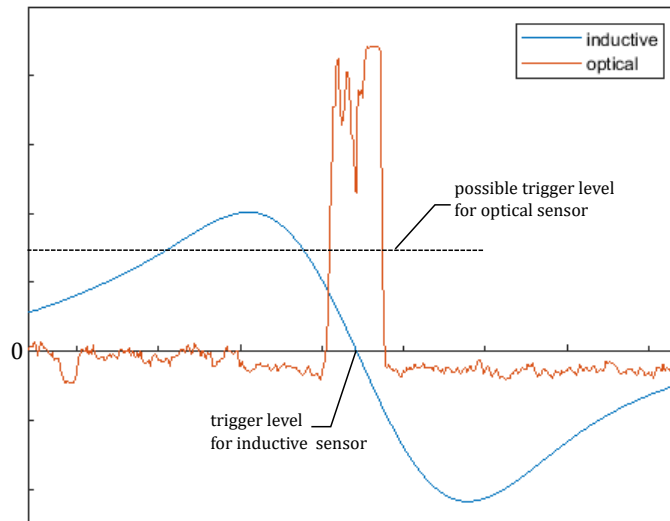


Figure 3.17: Typical plot of signals coming from inductive and optical sensors

the signal shape is possible to detect whether the blade tip is smooth and clean or dirty and rough. This feature seems useful for evaluating some kinds of damage to which the blades tips are subjected, but it carries its drawbacks. In fact, if the blade tip is too rough or dirty, the signal could be too ill-conditioned and this could lead to wrong TOA observations. An example of this situation is depicted in figure 3.18, where are compared the signals coming from a dirty blade tip (left) and a relatively clean blade tip (right): if the trigger level is chosen for instance in correspondence of 2 V there could be some extra blades in the final data due to the dirty tip of the first blade.

In order to avoid this type of problems is possible to change the trigger level or to use a trigger with hysteresis, which is able to ignore the noise coming from the blade's surface. Notice that these methods don't act on the shape of the original signal, so the informations on the tip surface conditions are still available.

A single optical sensor can be used also for measuring simultaneously both the tip signal and the OPR signal, if a mirrored tape is placed on the shaft in a position where the transmitted light reaches it. However this configuration can be used only in controlled environments like laboratories, because in practical applications it would not be reliable enough after few time.

Advantages

- Low spatial noise, which means low uncertainty of tip deflection
- Good spatial resolution
- Not sensitive to blade tip magnetization

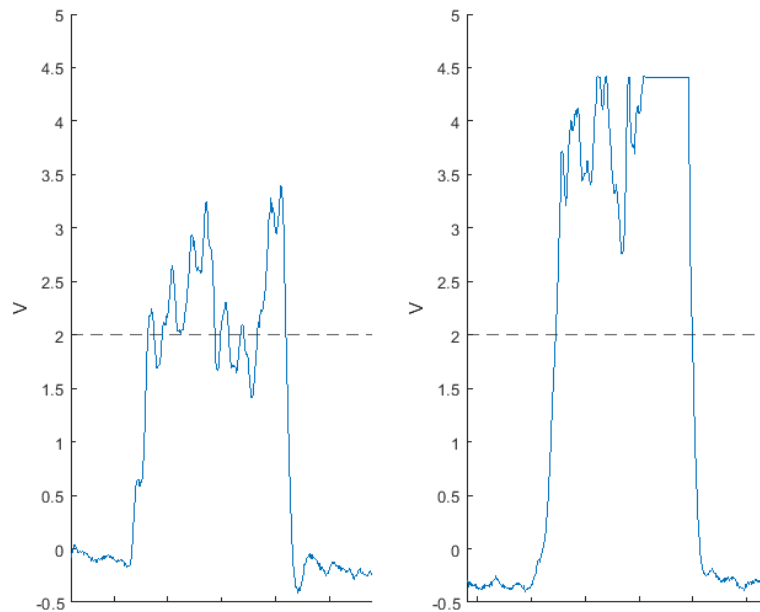


Figure 3.18: Effect of tip surface on the signal received by optical sensor

- Optical line sensors remove the uncertainty of steady axial movements
- The slope of the signal doesn't depend on rotational speed

Drawbacks

- High sensitivity to contamination and roughness of tip surface
- Low performance at high temperatures
- Higher costs with respect to inductive sensors
- Necessity of a laser generation unit
- Optical fibers are delicate to handle

3.5.3 Circumferential positioning

For what concerns synchronous vibrations, the circumferential positioning of the probes has an important role and there are two main points to focus on:

- Angle between first and last probe
- Spacing pattern between probes (uniform or non uniform)

Both will be briefly discussed in this section.

One of the most important considerations in BTT data analysis is the percentage of one cycle that is measured by the probes. If the percentage is too small, then significant errors can occur in the estimation of the response frequency. If the percentage is too large, then the response may be undersampled, again leading to large errors. The probe spacing on the resonance (PSR) is defined as

$$PSR = EO \cdot \frac{\gamma}{2\pi} \quad (3.16)$$

Where γ is the angle between the first and last probe. In figure 3.19 is clear that the low PSR data are not representative of the sine wave response. For this reason in practical

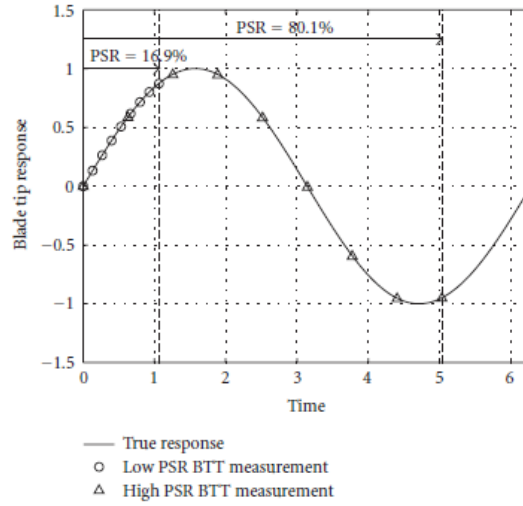


Figure 3.19: Effect of different values of PSR on the sampling

applications, if possible, the PSR is chosen between 40% and 70% for good results [17]. Furthermore the probe spacing should be set to give all samples within one wavelength of all predicted resonances.

Once the PSR is defined, it may be possible to choose also the spacing between the probes. Different patterns have been tested in the past and some of them are more suited for the purpose. A uniform spacing could give misleading results if the oscillation frequency is a multiple of the ratio

$$\frac{\text{rotational speed}}{\text{angle between consecutive probes}} \quad (3.17)$$

because in that case no vibration is recorded. That's why a non-uniform spacing between probes is preferable. In figure 3.20 is shown that samples coming from non-uniformly spaced probes are well representative of the vibration patch.

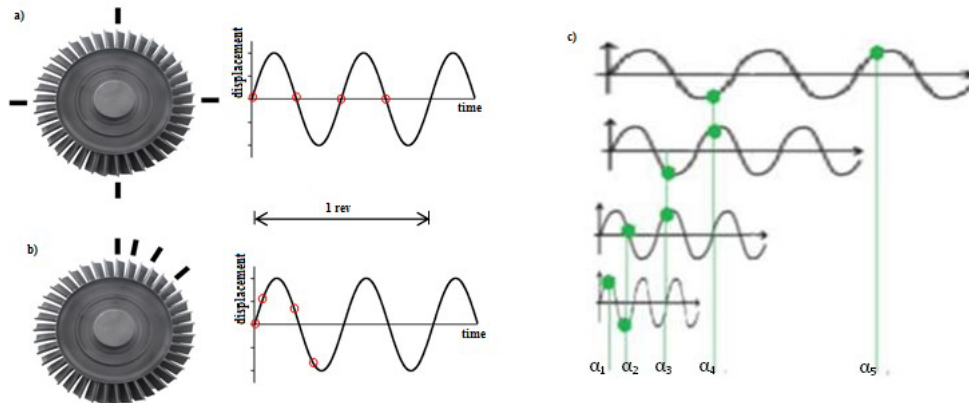


Figure 3.20: Effect of non uniform spacing between probes [4]

A uniform spacing is however mandatory in case of Fourier-based and Autoregressive methods.

3.5.4 Axial positioning

The finite element analysis is a convenient way to obtain the blade natural frequencies and the corresponding mode shapes, and the probe axial position is chosen in accordance with those mode shapes. It should avoid the node at which there is no displacement (see section 'Blade modes'). Given the blade axial movement, the probe axial position is selected usually near the trailing edge or the leading edge because in most of vibrations modes the largest displacements are located in correspondance of these zones.

But, as depicted in figure 3.21, it's not recommended to position the probe too close to these locations, in order to avoid the risk of missing some blades if the axial displacements are too wide.

When using more probes it's possible to position them in such a way that the measurements can represent also the steady axial movements discussed in section 3.4 [21].

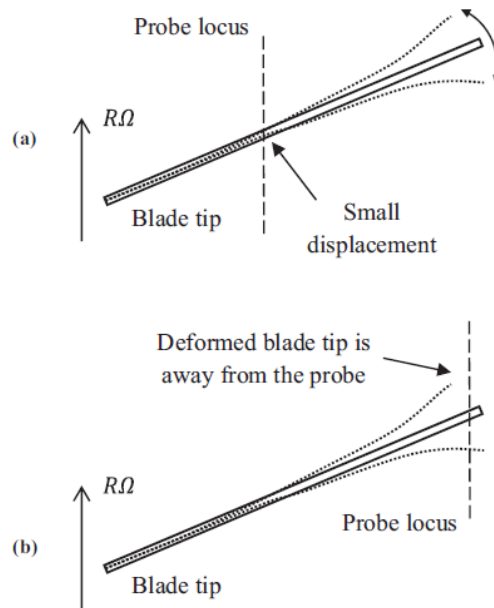


Figure 3.21: Risk of missing blade [22]

3.6 Hints on blade Tip Clearance (TC) measurements

One influent factor which impacts the efficiency of a turbomachine is the flow leakage over the tips of blades due to the presence of a certain clearance between blade tips and casing [31], in fact one of the design goals from the energetic point of view would be the minimization of this distance.

However, from the structural point of view there are many issues related to the fact that the distance blade-casing is not constant during the operation of the machine, mainly because of centrifugal force, thermal expansion, creep etc. This means that for safety it would be better to increase that space. Better monitoring systems of clearance would allow to use more strict tolerances and thus would lead to a better efficiency of the assembly with the same level of safety, that's why many techniques for measuring clearance in real time are still in development.

The most common sensors used for TC measurements are capacitive, but it comes out that some of the sensors used for BTT may be also used for TC, because whatever type of the sensor, when a blade passes in front of a probe an output signal is generated, and in most cases some features of such signal can be linked to the distance between the blade and the probe.

For instance in the case of inductive sensors it's possible, after proper calibration, to get the clearance from the peak to peak value of the signal [4], while for what concerns optical sensors it is more difficult to get such informations with a good accuracy.

Nonetheless there are many issues concerning the fact that the signal properties which depend on the clearance are also depending on other quantities involved, so it's not trivial to get an acceptable accuracy when using these sensors as clearance transducers.

In figure 3.22 is shown the plot of the peak-to-peak amplitude of a signal coming from an

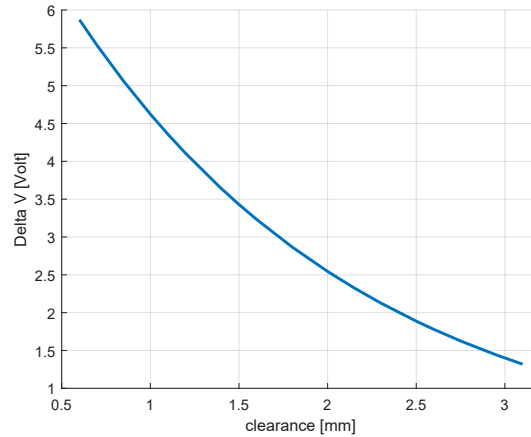


Figure 3.22: Typical plot of peak-to-peak amplitude vs clearance

inductive sensor as a function of the clearance. As expected the signal amplitude is higher for lower values of clearance, while tends to zero as the clearance increases. A similar behaviour occurs for optical sensors, but in that case it must be taken into account that the same output could come out for two different values of clearance (see figure 3.13).

In order to calibrate the sensors for clearance measurements a model is necessary. It's not trivial to find an appropriate link between the signal features and the clearance, because the physics involved implies non linear dependencies between all the variables that influence the system.

Notice that a system capable of measuring the clearance could be used also for the evaluation of rotor unbalancing.

3.7 Real time applications

The most ambitious objective of BTT systems is real-time monitoring of blades. Such a system in fact would be very useful in terms of safety above all, and would also lead to huge savings of time and money. In fact without a real time system the only way to evaluate the dynamic blade behaviour would be during engine overhauls.

Since 1986 some devices which used inductive sensors were developed in ITWL for this purpose.

The first one is called SAD (System Analizy Drganí) and was used to measure blade tip

displacement with respect to the blade root by means of two sensors fixed to the compressor casing or placed on a special steel frame in the turbine inlet. This technique was then upgraded to the so called SNDŁ (Sygnalizator Nadmiernych Drgań Łopatek), which uses two sensors in the compressor casing and warns the pilot of excessive rotor blade amplitudes during flight. One way to accomplish this task is to monitor the RMS value of the blades vibration amplitude.

A further unit, the SPŁ (Sygnalizator Pęknięć Łopatek), co-operates with the SNDŁ unit and automatically measures and traces blade vibration amplitude variations that may indicate the initiation and propagation of cracks.

In figure 3.23 is shown the layout of the installed devices. ITWL designed and installed

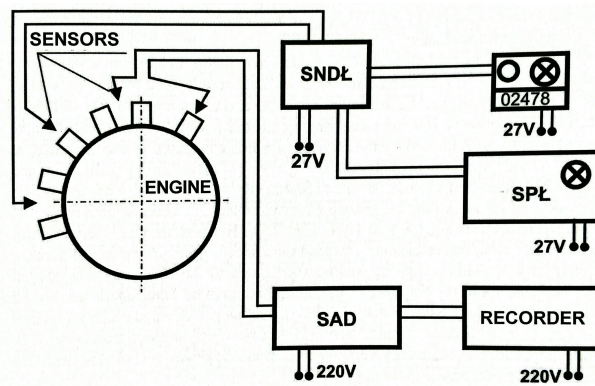


Figure 3.23: Arrangement of the SAD, SNDŁ and SPŁ measuring devices

similar devices in trainer combat aircraft jet engines with extraction as well as supersonic high-maneuvre aircraft engines [2] [3]. The systems are able to inform the pilot only about failures of higher priority and then advise him special procedure. Minor malfunctions and exceedances are reported only to ground personnel. Data from flights are transferred to ground database system in order to carry out further analyses.

Another significant real time application of tip-timing system is located at Bełchatów power station in Poland, where it is used as a tool for monitoring the blade vibrations of a low pressure steam turbine. Usually stationary engines are designed to work at speeds which are almost constant, but due to the presence of renewables in the energy mix in Europe, the steam turbines switched from a basic workload regime to a highly flexible system, as required by the national grid. This implies that the turbines, which have been designed many years ago, must be carefully monitored because they are not completely adapted to such a flexible mode of operation. The flexibility concerns the design of blades but not the speed, because that remains constant in order to guarantee the correct ac frequency.

The prototype of the system developed in ITWL has been running continuously in the power plant network since early 2017 and it has progressively improved. It enables to

avoid the blade's operation with increased vibrations, improving the LPT reliability and reducing the repair costs.

For any system involving bladed disks the results of real-time vibration measurements and numerical calculations could be used to optimize unit operation, in particular it is expected that the costs of maintenance will be reduced mainly by:

- increasing the mean time between failures;
- reducing the frequency of inspections which would imply a shutdown of the plant

Chapter 4

Characterization of fan blade vibration

4.1 Description of the system

In this thesis work it has been studied the dynamic behavior of a rotating assembly which was part of a wind tunnel.

The system consists in a wooden panel on which are mounted four fans that a few years ago were used in order to generate the air flow necessary for the wind tunnel to work. The fans are set in motion by four synchronous three-phase electric engines, which can provide a maximum rotational speed of 1600 rpm each when on the rotors are mounted 4 blades.

It was seen that in the case of 8 blades the maximum speed allowed is about 1200 rpm.

In the nominal conditions, when installed on the wind tunnel outlet, the rotational speed is 1400 rpm, with a flow of 9380 m³/h and a power consumption of 0,55 kW for each rotor. The original power inverter was not available and so it was used another model of inverter which worked as well.

The tests were performed on only one of the four rotors, because there was only one device available for the control of speed.

In order to control the rotational speed it was necessary to use a power inverter which was installed between the grid and the engine. The inverter has a small screen and an analog handle that were used in order to set the acceleration and deceleration of the engine and its maximum speed (figure 4.1).

It was chosen an acceleration of about 3.6 rpm/s and the same value was employed for the deceleration, resulting in the plot depicted in figure 4.2. This value of acceleration is not the minimum allowed by the power inverter, but it is acceptable according to the experience of previous tests performed in ITWL on different systems by other people.



Figure 4.1: Front panel of the inverter

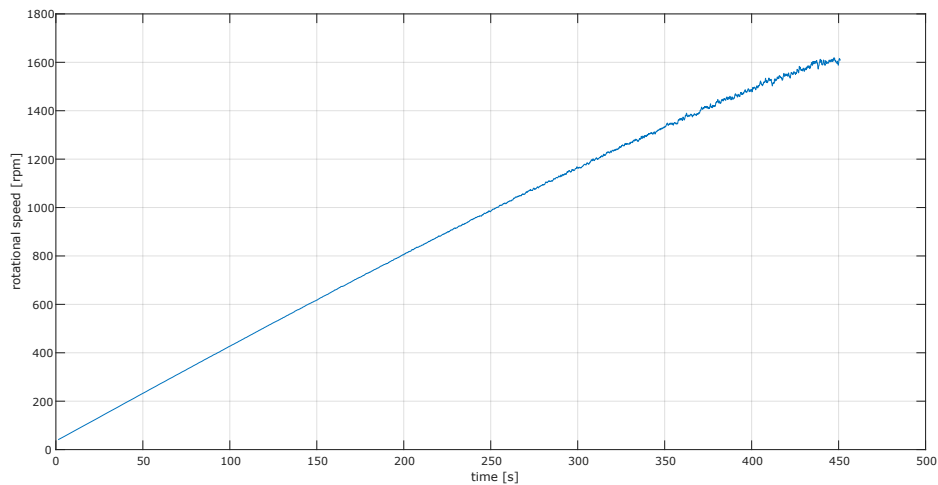


Figure 4.2: Rotational speed versus test duration

The whole assembly (panel + rotors) was set for the first test in a small room that was available for the installation of sensors and for the execution of the tests in different days. The position of the panel was therefore much different than its design purposes. In fact in this case the airflow streaming through the panel holes doesn't have a principal axial direction at the inlet, but the air comes through the bladed disk with a more random distribution of velocity.

This fact implies two important consequences:

1. The speed acceleration is not uniform, because at high angular velocity the turbulence is so strong that affects heavily the dynamic behaviour of the rotor.
2. There is no possibility to mount obstacles that could provide a known excitation of a frequency of N engine orders (with N the number of eventual obstacles).

For what concerns the first drawback of the panel positioning it can be seen from figure 4.2 that as the speed increases the rotor has trouble in maintaining the value imposed by the power inverter, which by itself gives a precise linear increase of frequency in output.

The second drawback was tested, and the two attempts of introducing some clogs at the inlet turned out to be completely useless, since the normal airflow was not regular enough to be affected by any kind of obstacle.

For the second test involving more sensors it was possible to mount the frame in its original position at the inlet of a wind tunnel, as described in section 4.3.3. In this way it was also possible with that test to see the effects of an obstacle on the blade vibrations.

4.2 Finite element model

4.2.1 Geometry acquisition

Blade

In order to create the numerical model of the blade and subsequently of the whole assembly, it was needed to acquire in some way the geometry of the blade. ITWL is equipped with a tomograph which could be used for this purpose.

A correct CT (computed tomography) requires some shrewdnesses in order to get a 3D scan which is accurate enough. In fact the blade is bigger than the average objects analyzed by this device and it was required a proper support (in terms of material) and a multiscan procedure in order to get a CAD geometry that could be subsequently used for a finite element model.

The power of the X-ray lamp had to be adjusted so that it could detect the blade material from any angle, this is not a trivial task because the thickness changes a lot depending on the point of view.

From the tomography it's possible to notice if the object has internal faults or layers of different materials, in this case it seems that there are not internal faults (figure 4.3).

Once the scan procedure finished, the data were processed by a computer in order to isolate the material of the blade from the support material, then exporting the file in .STL format. In this way the CAD geometry consisted in a main surface composed by about 687000 triangles and few small surfaces coming from air bubbles present in the glue used

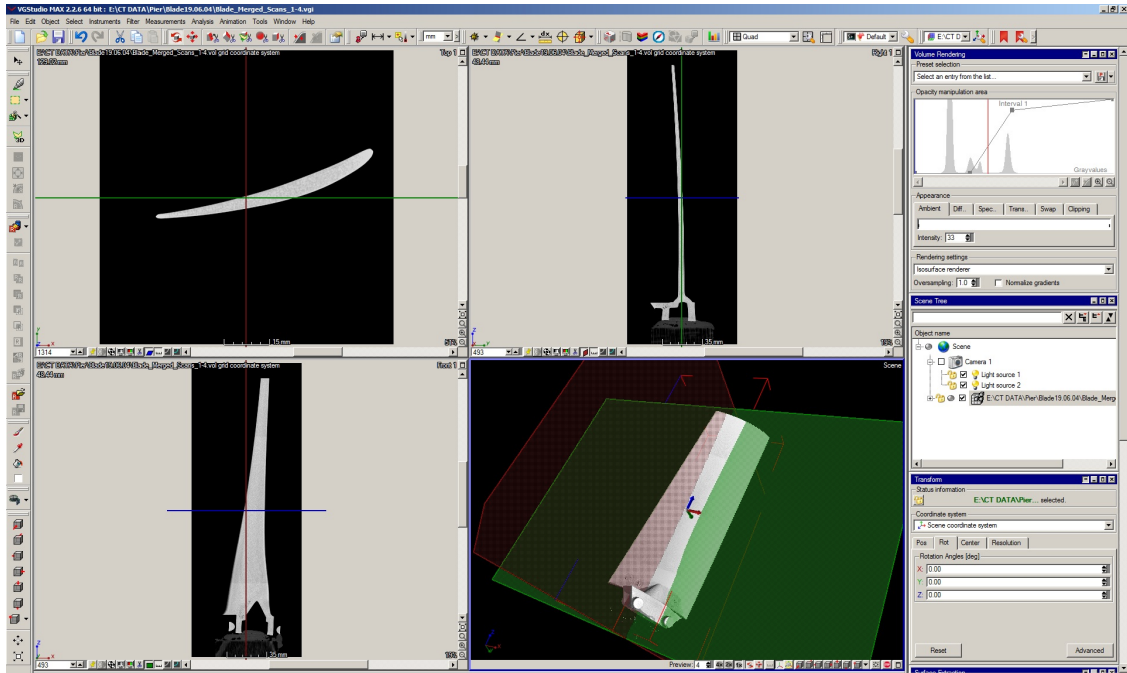


Figure 4.3: Sections of the scanned blade

for attaching the blade to the wooden support.

In the current state the model could not be imported in ANSYS for the finite element analysis, that's why some work was needed in order to clean the geometric mesh from the unnecessary surfaces and reduce the number of facets.

Two software were used for doing that: MeshLab, an open source mesh editor, and Solid Edge, exploiting the temporary student license. In particular MeshLab was used in order to clean the mesh removing the unnecessary parts which caused the errors and Solid Edge, with its reverse engineering features, allowed the simplification of the final mesh, which at the end of the process consisted of only 36 simple surfaces (planes, cones, cylinders and b-splines). In figure 4.4 it is possible to see how the edges of the blade are much better defined after the manipulation, while in figure 4.5 is shown the whole blade.

Rotor

The geometry of the rotor was much more simple to get, because it could be considered as an axisymmetric body. The dimensions were taken by hand with a caliber and then the CAD model was made using Solid Edge.

The rotor itself consists in two aluminium plates bolted together in order to fix the blades in the correct position. When the bolts are tightened the plates get in touch, so for the geometry they were considered as a unique body.

Some small simplifications were made in order to obtain a more regular mesh during the

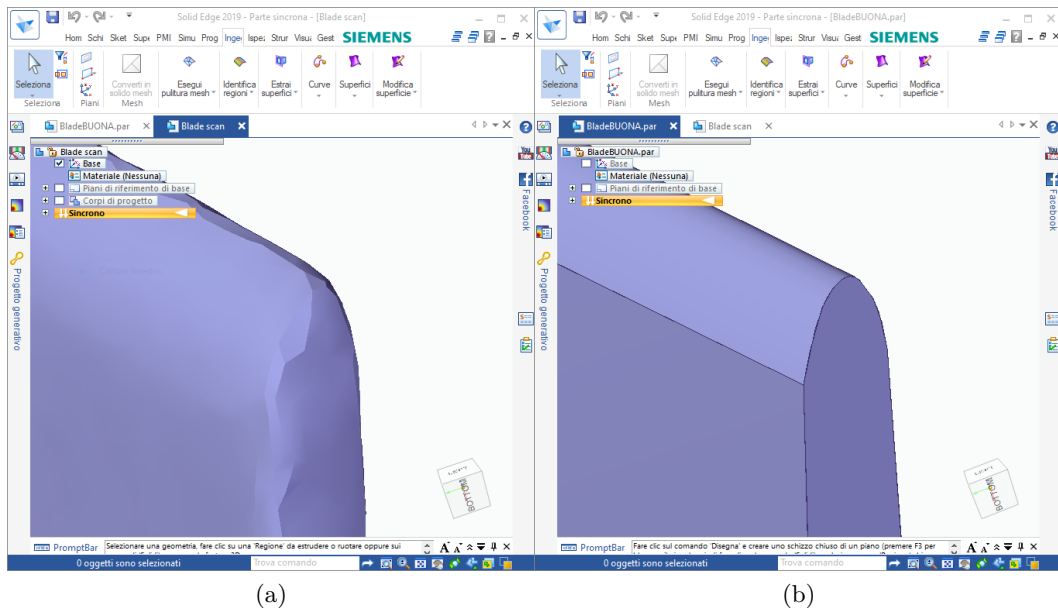


Figure 4.4: Detail scan on the blade tip (trailing edge) (a) Clean mesh before manipulation, (b) Final geometry

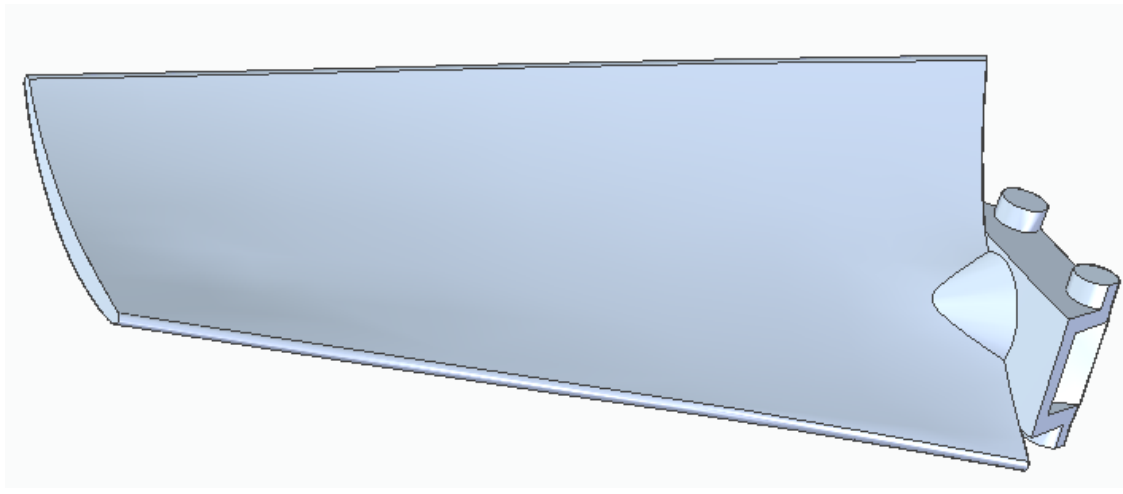


Figure 4.5: Final simplified geometry of a single blade

finite element modelling, for example the holes for the bolts were removed, being their diameter much smaller than the average dimension of the plates.

In figure 4.6 a side view of the rotor is visible, with its section highlighted. The blades are not fixed just by the pressure generated by bolts, but in order to hold them in place and guarantee a correct alignment there are some cavities in both plates where the four protrusion in each blade root can fit precisely (figure 4.7).

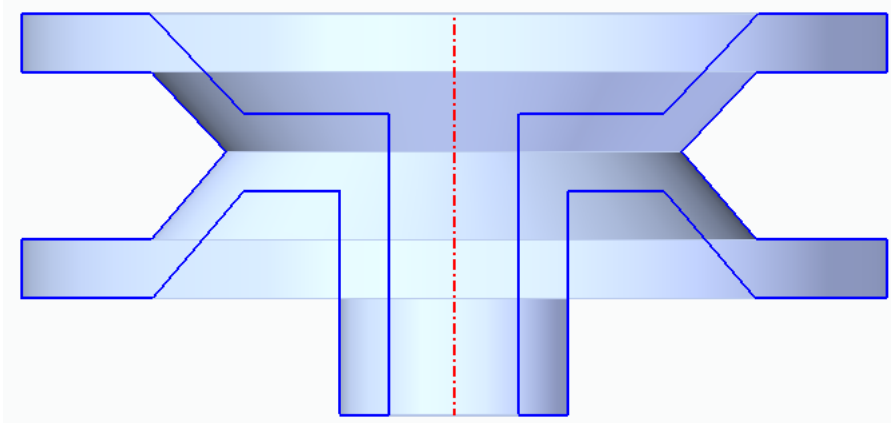


Figure 4.6: Rotor section; when the blades are mounted their roots are clamped between the two plates

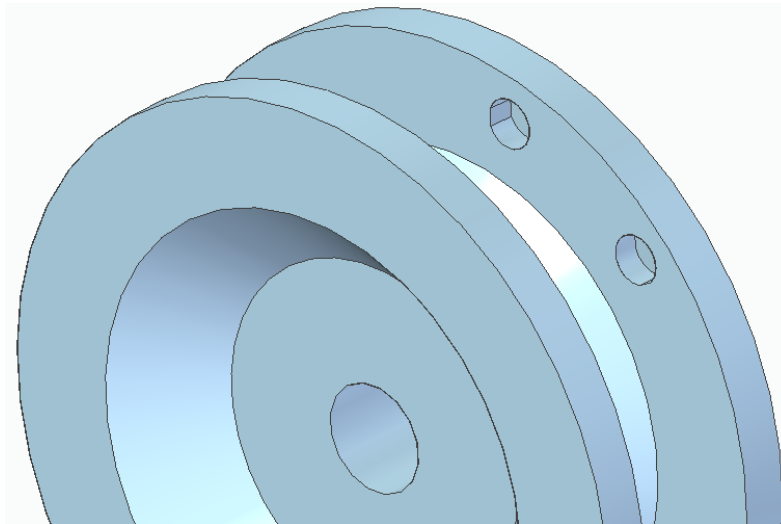


Figure 4.7: Detail on the cavities located in both plates

4.2.2 Material uncertainties

The material of the blades is a glass-fiber reinforced PPG (polypropylene glycol) manufactured with injection moulding, while the material of the rotor plates is an aluminium alloy. In order to obtain detailed informations about the materials of the blades and the rotor, the company who manufactured them has been contacted, however the only information that they could give was the value of the flexural modulus of PPG, which for homogeneous and isotropic materials coincides with the elastic modulus.

In this case the manufacturing of the blade suggests that the fibers contained in the polymer have a preferential direction, leading to a globally anisotropic behaviour and thus to

an elastic modulus different from the flexural modulus. Anyway, the evaluation of the correct local elastic properties in such situation is very difficult, also because there wasn't any information on the fibers length and volume percentage. Thus the elastic modulus was considered constant in all the blade and equal to the value of flexural modulus provided by the manufacturer, assuming an isotropic and homogeneous material.

For what concerns the density, it was obtained simply by using the volume computed in the CAD software and the weight measured with a scale. Notice that this value corresponds to the average density, which in reality may not be correct in all the points of the blade.

However it was assumed that the injection moulding process was executed properly, leading to a material with globally uniform density. With this assumption the average density can be used as a constant value valid in all the blade's volume.

The hypothesis of correct injection moulding is in some way confirmed by the tomography, because it shows no air bubbles inside the blade.

Another important dynamic property that wasn't available is the damping. Usually polymers can be considered viscoelastic materials and thus are characterized by structural damping which depends on the vibration frequency. In order to obtain such a quantity it's necessary to perform many experimental tests, which were not available.

Anyway the numerical simulation was executed many times for different values of constant structural damping coefficient, leading to very small variation in the results. The probable reasons of such a behaviour will be explained better in the section related to Campbell diagram and convergence.

4.2.3 Blade model

For the finite element modelling the software used was ANSYS Workbench 2019 R2, student version. The procedure consisted in two steps: first the modelling of a single blade in order to obtain its mode shapes and the Campbell diagram, then the modelling of the whole assembly needed for some considerations about coupling between blades and nodal diameters.

After the material definition, discussed in the previous section, the next step is the geometry definition. ANSYS allows to import CAD files for that purpose and in order to do that properly it was necessary to do three important tasks:

1. Modify the reference frame
2. Slice the blade in two separate parts
3. Change the file format

The reference frame had to be modified because of convenience in the definition of the rotational speed of the blade. In fact when a Campbell diagram is needed it is necessary

to define the axis of rotation of the system analyzed. The speed definition could be made by components or by geometry definition, and for convenience it was decided to use the first approach.

If the reference frame is random, the vector used as axis of rotation of the blade has a component in all directions x, y and z . Instead if the reference frame is properly rotated it is possible to make the axis of rotation coincide with a reference axis.

In this case it was decided to modify the reference frame so that the blade's rotation could be defined by the z component only.

For the other two axes, a convenient choice is to make one of them coincide with the tangential direction of the blade. That is because in this way after the mode shapes are found it's possible to decompose the displacement components in the reference directions, and in BTT systems the tangential component has fundamental importance. The x axis was chosen in this way, and the y axis is directed towards the blade, as depicted in figure 4.8. The slicing of the blade was necessary in order to have a mesh as much regular as possible.

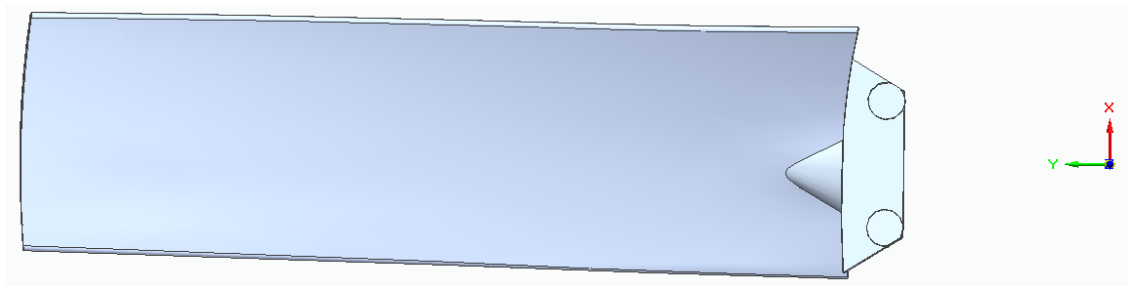


Figure 4.8: View of the reference frame used in the model

In fact ANSYS allows the choice of different meshing methods, each one is more suitable for a specific type of geometry.

It's always convenient to choose a method which provides regular elements, because in this way the distortion error due to the Jacobian ratio is minimized.

Furthermore it is known from the theory that brick elements are usually preferred to tetrahedrons, because they allow higher orders of the shape functions used to interpolate the displacements. This leads usually to better accuracy in the deformation and stress evaluation, even though that's not a universal rule.

In this case the shape of the airfoil seems very suitable for being meshed with brick elements, and so in a first attempt a mesh method based on bricks was set.

During the meshing process a problem occurred in the root of the blade, because there the geometry is much more complicated than in the airfoil and thus a uniform brick mesh cannot be executed.

A second attempt on the choice of the meshing method was made by using all tetrahedrons

of order 2, because this type of element is very well suited for complex geometry. Even though in this case the meshing process succeeded, it was evident that the number of nodes was too high and it could not be possible to make more tests with different element sizes for the convergence verification.

A mesh with tetrahedrons of order 1 could be set, but from the finite element theory is well known that linear tetrahedrons make the model stiffer than the real component, so they are used only for very simple geometries and loads, which is not the case. Anyway, this option could be used as a last resort if the other choices would fail.

At this point it was decided to slice the blade in two different parts, applying on each of them a different meshing method. The final result is depicted in figure 4.9. For the

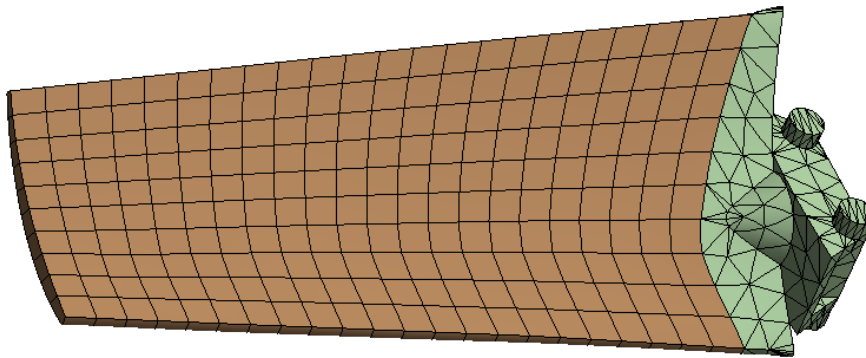


Figure 4.9: View of the reference frame used in the model

airfoil the element type chosen is brick SOLID186, while for the root it was chosen the tetrahedral element SOLID187 (figure 4.10). Notice that both are quadratic because they present a node within every edge, this choice is explained later in the Campbell diagram paragraph, and it's related to convergence issues. Moreover, it has to be noticed that the brick element has 20 nodes whilst the tetrahedral element has 10 nodes, so at first sight one may think that a tetrahedral mesh would decrease the number of nodes. However, if the airfoil is meshed with tetrahedral elements, in order for them to be regular enough it is necessary to use a much smaller size than the one allowed by brick elements, so the number of nodes increases.

With this configuration it was possible to make different simulations as explained in the following.

After the choice of the element type there are other two important parameters to be set:

- Element size
- Element order

The constraints which guided the choice of these two parameters are:

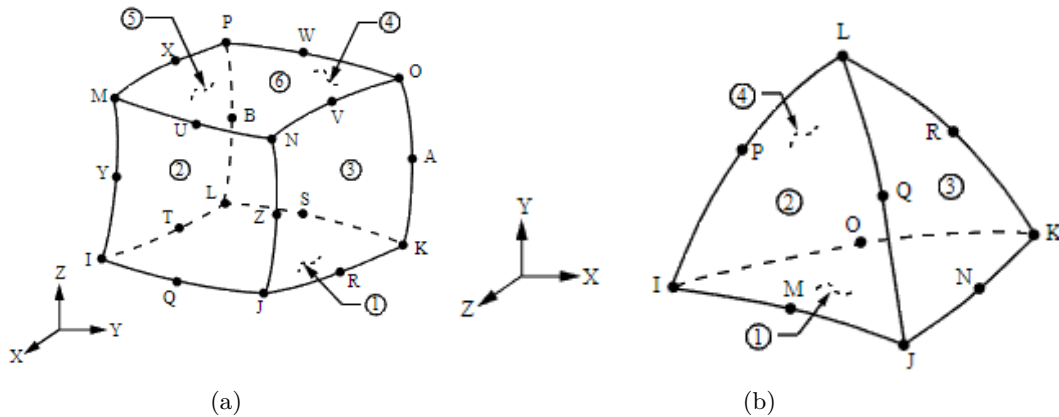


Figure 4.10: (a) Quadratic brick element SOLID186, (b) Quadratic tetrahedral element SOLID187

1. The maximum number of elements (and nodes) allowed by the student license, equal to 32000 items
2. The accuracy of results

Of course in order to stay within the maximum number of nodes it is convenient to choose big elements of lower order, however there is also an upper limit to the element size given by the thickness of the blade.

The accuracy of results acts in the opposite direction of the first constraint, in fact in order to obtain more accurate results it is suggested to use small elements of higher order.

Even though it is possible to use a variable sizing of the elements, after few attempts it has been evident that the maximum allowed size is 9 mm.

The lower size limit instead depends on the maximum number of nodes allowed, in this case it has been verified that the minimum size that can be used is 5 mm.

The final choice consisted in quadratic elements with maximum size of 9 mm.

Convergence at zero speed and element choice

The convergence verification has been made at zero rotational speed and with no damping. The simulations could be executed with different element sizes and orders, and the values of the fifth undamped natural frequencies (in Hertz) in all the cases are reported in table 4.1.

Higher frequency modes are more affected by the errors due to the finite element stiffening, because they involve more complex displacements that are difficult to be represented well by the shape functions. This means that if there is convergence of the highest considered frequency also the other frequencies will converge. This has been verified, even though in

table 4.1 only the fifth natural frequency is reported for the sake of clarity.

	size [mm]	order	
		linear	quadratic
fifth natural frequency [Hz]	5	721.23	685.98
	7	735.53	687.35
	9	743.23	688.34
elements	5	2735	2950
	7	1332	1578
	9	1046	1400
nodes	5	2213	9623
	7	1065	4916
	9	779	4013

Table 4.1: Results of the simulations conducted for the convergence check

It is possible to notice that, as expected, linear elements are not suitable because their use implies a numerical stiffening of the system which is not negligible. In fact the difference in the natural frequency computed with linear and quadratic elements is about 35 Hz in the best case (corresponding to the element size of 5 mm).

Once the order of the elements has been established, it is necessary to choose a size. For that purpose it is useful to plot a graph of the natural frequency versus the number of nodes (figure 4.11), because this last value is directly linked to the number of equations that the processor has to solve and thus indicates also the time required for the computations. This graph makes evident that it would be pointless to use elements with size 5 mm, because the increase in the number of nodes is much more influent than the change in the natural frequency. In fact with 4013 nodes the frequency value is equal to 688.34 Hz, while with more than double the number of nodes (9623) the frequency value is only 2.37 Hz lower, with a relative error of about 0.3% between the two results.

From this consideration the final parameters of the elements were:

- Element size: 9 mm
- Order 2

Modal analysis settings

As previously stated, the desired output results are the modal shapes of the blade and the Campbell diagram. In order to obtain them it is necessary to set a few analysis

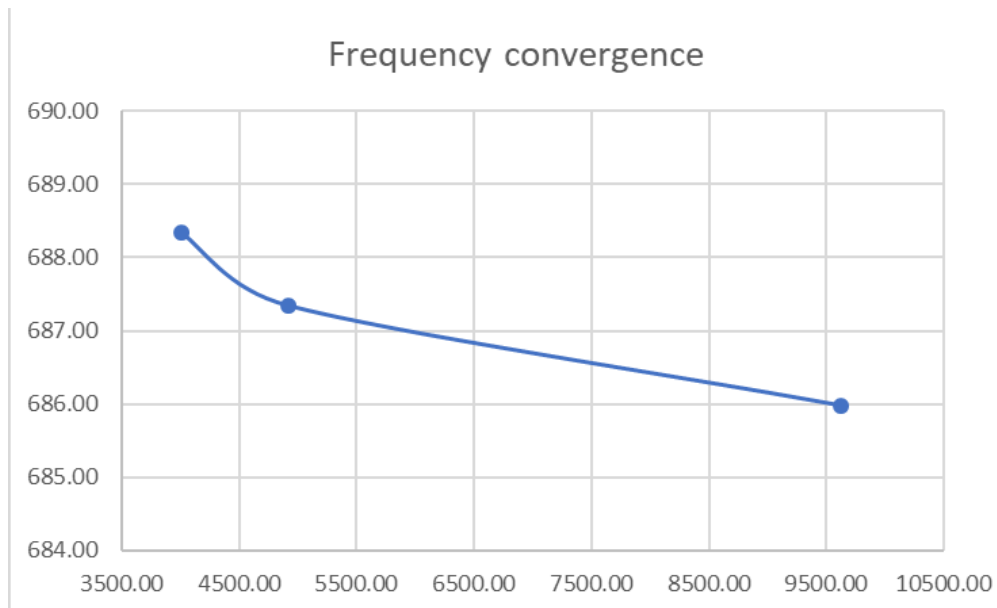


Figure 4.11: Plot of the 5th natural frequency versus the number of nodes

parameters, such as the constraints and the rotational speed range.

Constraints The definition of constraints is never a trivial task, and also in this case some assumptions had to be made in order to go ahead with a proper model.

In fact the blade roots are kept in position by both the pressure of the plates and the centrifugal force that acts during the rotation of the assembly. Their influence changes with the rotational speed, so a precise model is very difficult to manage.

For the sake of simplicity it was considered that the blue surfaces (on both sides of the root) depicted in figure 4.12 are always in contact with the plates and also that the interfaces do not slide each other. A further approximation for the model was to consider the rotor as

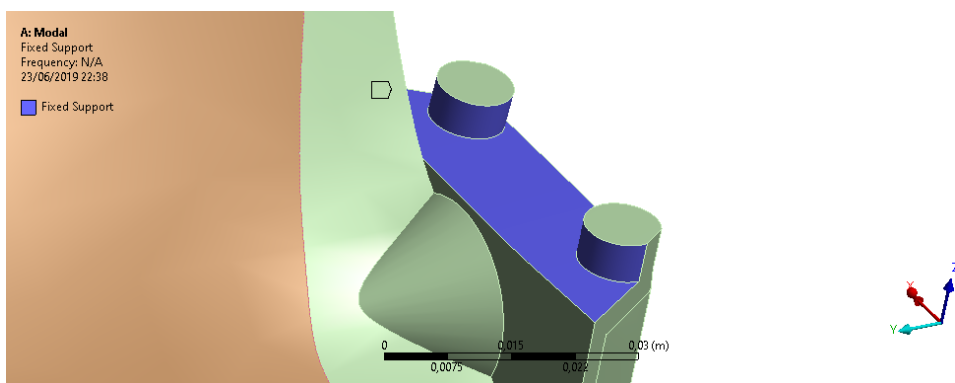


Figure 4.12: Detail on the surfaces used as fixed support for the blade

perfectly rigid, but this assumption makes more sense because the rotor’s material is much stiffer than the blade’s material.

From these assumptions it comes out that a fixed support constraint could be a valid choice for the already mentioned root surfaces.

Rotational speed In order to apply a rotational speed to the blade it is necessary to define its direction and magnitude. For what concerns the direction, it was possible to define it coincident with the z axis because, as explained in section 4.2.1, the blade’s position in the global coordinate system was chosen for this very purpose.

For what concerns the magnitude, the engine is limited to rotate at approximately 1600 rpm, that means a maximum angular velocity of 167 rad/s.

For this reason, and knowing that usually the natural frequencies don’t change very much with the speed, it was chosen a speed range within 0 rad/s and 170 rad/s with 10 intervals on which compute the eigenvalues and eigenfunctions of the blade in order to plot its Campbell diagram.

Modal shapes and natural undamped frequencies of the blade

Since the damping was unknown, the modal analysis was performed considering the undamped blade. It is known that the damping affects the value of natural frequencies, but usually its influence is negligible from that point of view. In fact after the first analysis other simulations have been made considering different constant structural damping ratios, and they showed that the variation of natural frequencies was really small compared with the value of the frequencies themselves.

In figure 4.13 are represented the first five mode shapes obtained from the model. The corresponding natural undamped frequencies are listed in table 4.2, but only for the non rotating blade for sake of simplicity. The variation of the natural frequencies with angular velocity is shown in section 4.2.4, figure 4.14. In the images of figure 4.13 the lower

ω_{n1}	ω_{n2}	ω_{n3}	ω_{n4}	ω_{n5}
70,824 Hz	285,43 Hz	352,38 Hz	521,29 Hz	688,34 Hz

Table 4.2: First five natural undamped frequencies of the non rotating blade

side of the blade corresponds to the leading edge, while the upper side is therefore the trailing edge. This fact had to be highlighted in order to notice the problem explained in section 2.1, which involves the nodal lines intersecting the blade’s tip.

In particular for the detection of displacements related to mode 3 it becomes evident that the sensor should not be positioned near the leading edge, for there is a nodal line and the displacement will be zero. The same reasoning applies to modes 2 and 5 with respect to

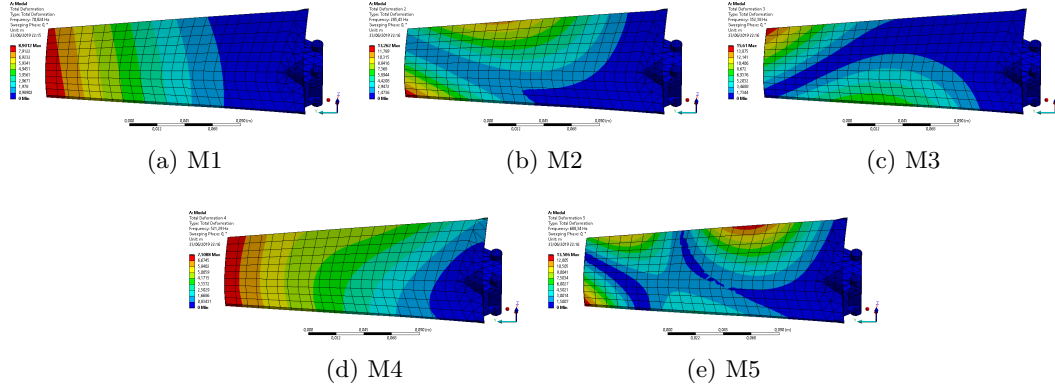


Figure 4.13: Mode shapes of the blade according to the FE model

the trailing edge.

4.2.4 Campbell diagram of the blade

The solution obtained by the FE model includes also the Campbell diagram of the blade plotted using the 10 speed chosen in the range $0 \div 170$ rad/s. These values were imported in MatLab in order to interpolate them and check the intersections with different EO excitations (figure 4.14). In figure 4.14 the first consideration that can be made regards the

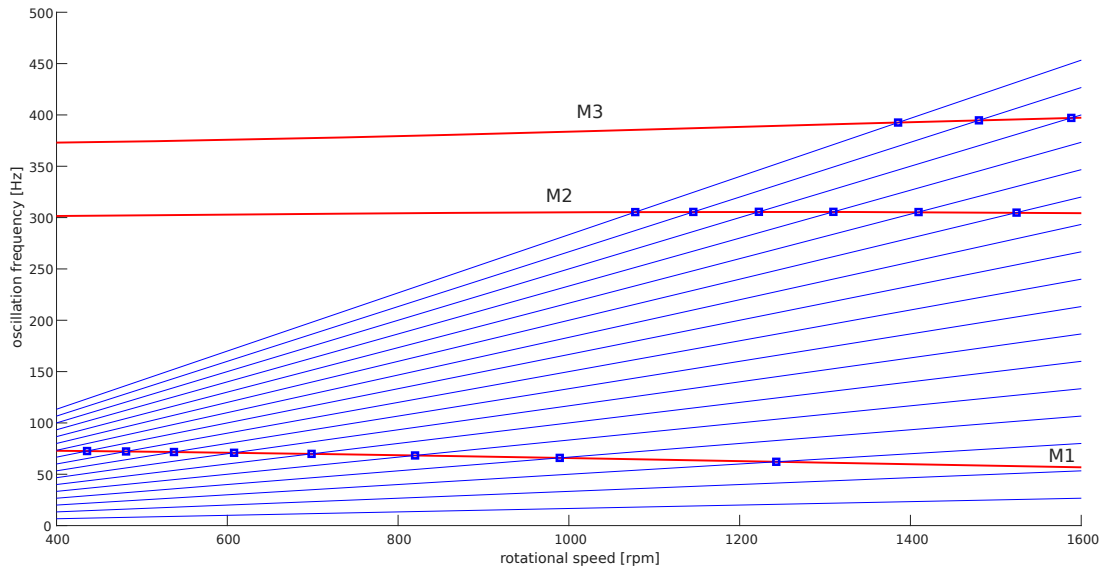


Figure 4.14: Campbell diagram obtained from the FE model, the blue lines represent EO excitations from 1 to 17 while the red lines represent just the modes from 1 to 3 for clarity

natural frequencies of the blade, which as expected change only slightly with the rotational

speed. This confirms that the choice of defining only 10 values of rpm for the solution was sufficient.

Furthermore it is noticeable that the intersections are very close for what concerns modes 2 and 3, while for mode 1 the intersections are much more distinguishable, in particular at high speed. In this situation is almost impossible to isolate eventually a single mode vibration at a certain speed, because for every value of speed there are different EO excitations that intersect more than one mode, which is the case of multiple synchronous vibrations. Even though synchronous vibrations can occur, it could be possible to neglect one or more of them during the signal analysis. This is because the displacement measured by BTT system are only in the x direction, but not all modes affect these displacements in the same way.

In fact in the modal analysis of a structure it is important to consider the modal participation factors, which give an indication on how much every mode affects the displacements in a specific direction. In figure 4.15 there is a table from the ANSYS output file in which the modal participation factors in x direction are exposed. The most interesting part of this

***** PARTICIPATION FACTOR CALCULATION ***** X DIRECTION							
MODE	FREQUENCY	PERIOD	PARTIC.FACTOR	RATIO	EFFECTIVE MASS	CUMULATIVE MASS FRACTION	RATIO EFF.MASS TO TOTAL MASS
1	70.4983	0.14185E-01	-0.11737	0.939015	0.137767E-01	0.280837	0.150428
2	285.810	0.34988E-02	0.98470E-01	0.787774	0.969626E-02	0.478494	0.105873
3	352.911	0.28336E-02	0.71319E-01	0.570568	0.508647E-02	0.582181	0.555391E-01
4	521.902	0.19161E-02	0.12500	1.000000	0.156243E-01	0.900680	0.170602
5	688.756	0.14519E-02	-0.69801E-01	0.558423	0.487223E-02	1.00000	0.531999E-01
sum					0.490560E-01		0.535642

Figure 4.15: Modal participation factors in direction x

table is the last column, where are listed the values of the actual mass that participates in the vibration for each mode in direction x. From these values it results that mode 3 and 5 influence the x displacements much less than other modes, but not so much that they can be neglected.

Anyway, from a study carried out by Dimitriadis [18], it comes out that as the damping increases it becomes more difficult to distinguish synchronous vibrations that occur at slightly different rotational speeds. In our case, in addition to the fact that the intersections between EOs and natural frequencies are close, also the damping, even though it is unknown, is surely much higher than it would be for metallic structures. This means that our efforts to isolate eventual synchronous vibrations will probably fail, also because the airflow is not guided and the room in which the measurement test were performed was small, so in addition to the absence of guided vanes there was a lot of turbulence, as already explained in section 4.1.

4.2.5 Assembly model

After the single blade modal analysis, in order to see the nodal diameters described in section 2.2.

For this model it was exploited the axisymmetry of the system, therefore the geometry used consists in a quarter of the whole bladed disk, as depicted in figure 4.16 (a). Figure 4.16 (b)

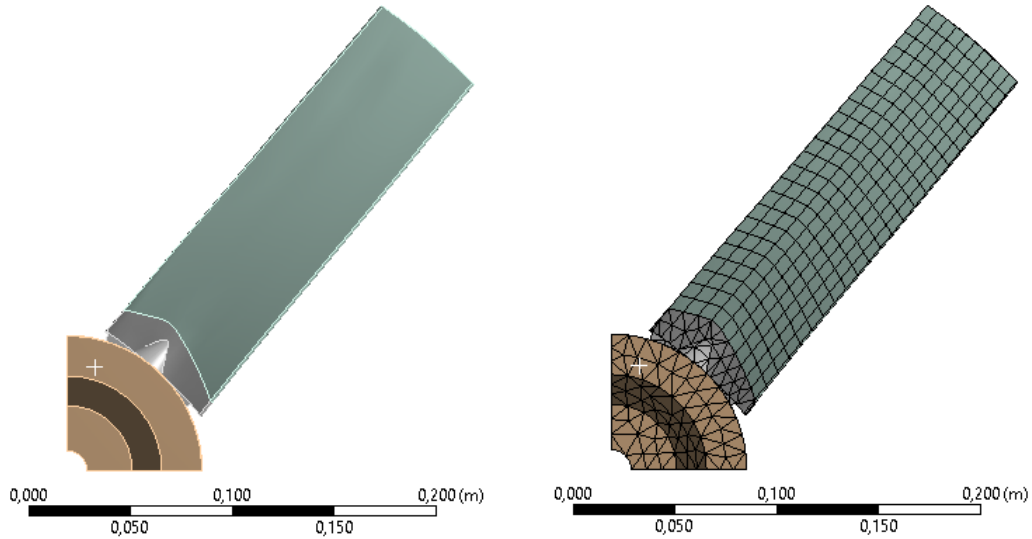


Figure 4.16: Geometry of a quarter of the assembly, used by the ANSYS software for meshing

represents the same geometry after the meshing process. It is possible to notice that for the disk has been used the same type of element employed in the blade root's meshing, for two main reasons:

1. The rotor is much more stiff than the blade, so the displacements will be negligible when compared to the blade's ones even if we used brick elements
2. For the type of constraint used it was necessary to use tetrahedral elements at the interface with the blade's roots, and a smooth transition from tetrahedra to bricks was not allowed by the rotor shape

The total number of nodes required for the meshing of this geometry is low enough to guarantee that the complete mesh will not exceed the maximum number of nodes allowed by the ANSYS student license, so it's not needed to change the element parameters previously used for the single blade model.

Some assumptions have been made for defining the type of constraint between the blade and the rotor plates: it was chosen to consider the blade root bonded with the rotor cavities, with no sliding allowed.

This condition is different than the fixed support chosen in the single blade modal analysis, but due to the higher stiffness (aluminium is much more stiff than glass-fiber reinforced polypropylene) of the rotor with respect to the blade it will not imply big problems.

From these assumptions it seems that the assembly analysis could also be performed considering a perfectly rigid rotor, but that's not the case, because in order to visualize the nodal diameter it is necessary to take into account a sort of coupling between the blades, given by the rotor stiffness.

The simulation was executed also this time considering the undamped system.

As there are only four blades in the whole assembly, there are only two symmetry planes and therefore, as explained in section 2.2, only shapes with up to two nodal diameters will come out from the simulation.

In figure 4.17 three disk modes are shown, all corresponding to the first bending mode of the blades but with different values of nodal diameters: from 0 to 2. The difference between

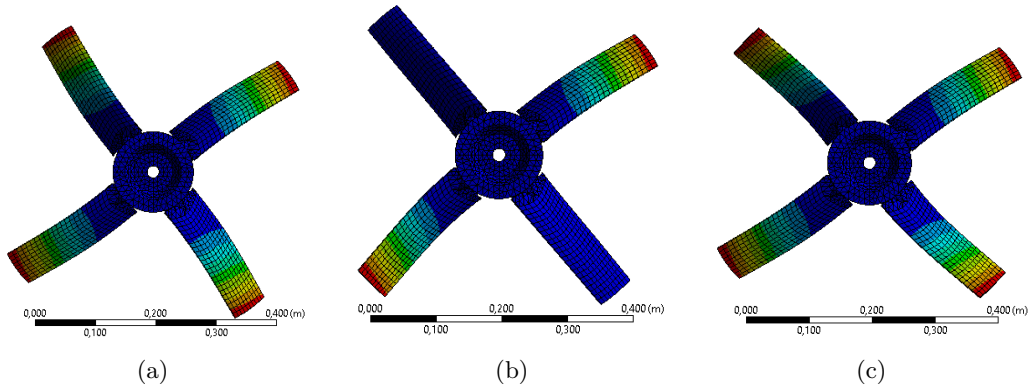


Figure 4.17: Mode shapes of the assembly according to the FE model

(a), (b) and (c) is only the phase between the blades' oscillations. In (a) the phase is 0, in (b) it's $\pi/2$ and in (c) it is π .

The number of symmetry plane defines the maximum number of nodal diameters that it's possible to have without ambiguities, in fact between two consecutive nodal diameters the phase changes by $\frac{\pi}{n^o \text{ of symmetry planes}}$.

In particular, in (b) the nodal diameter is aligned with two opposite blades, which in fact present zero displacements on the whole length. An important observation can be made regarding the first natural frequency of the assembly. Its value is 71,24 Hz, very close to the first natural frequency of the single blade.

This is an expected result because as already stated the stiffness of the rotor is much higher than the one of the blade, so it is natural that the first resonance doesn't change much.

4.3 Measurement system and results

Two tests were performed with different configurations:

- One optical sensor for detecting blades and eddy current sensor for OPR reference
- Six inductive sensors for detecting blades and optical sensor for OPR reference

In this way it was possible to verify some features of different types of sensors that are described in section 3.5, and to understand better the advantages of using more probes.

4.3.1 TOA extraction from raw data

In order to extract the time of arrival of the blades (and of course of the rotor notch) from the acquired data it was necessary to process properly the signals. This task was accomplished by developing a suitable MatLab code.

The first requirement for the detection of TOAs from any signal is the definition of the triggering level, which is the voltage threshold that the signal has to exceed in order for the system to detect the passage of a blade (or the passage of the notch, for the opr).

In order to avoid noise issues the trigger has to be hysteretic, which means that it has to maintain its value for a certain time after the threshold is exceeded. In this way it is possible to avoid the undesired phenomenons of missing blades and extra blades that could generate big errors in the computation of tip displacements.

The system then has to record the times at which the trigger changes sign in order to obtain the desired time of arrivals.

The procedure seems easy, but in this case there are a few additional difficulties to overcome:

1. The speed of the assembly is not constant, so the hysteresis value of the trigger has to be chosen carefully in order to be working for any speed
2. In the case of optical sensor, two different values of hysteresis have to be used for the two positions
3. The noise generated by the power inverter affecting the OPR signal has to be taken into account

A test with approximate duration of 450 s with two channels sampled at 500 *kHz* each gives two data vectors of doubles with a length of about 225 million elements each.

Considering that the speed increases linearly from 30 rpm to 1600 rpm, the number of revolutions made by the rotor is equal to 6112.5, corresponding in our case to 24450 blades' passages.

This means that the interesting points of both signals amount to only 30000 units. That's the reason why it was necessary to implement a method that could extract these points in an efficient way, without the necessity to make useless and time consuming complex computations on the whole data set involving 450 million samples.

The only operations made on the whole vectors consisted in two element-wise products for each set (shifted by the correct amount corresponding to the threshold). If a vector v is multiplied by a shifted copy of itself, the resulting vector has positive values everywhere except in the positions where the original signal has a sign change. This can be written in the following way:

$$v(z) = v(z), z : v(z \pm 1) \cdot v(z) < 0 \quad z = 1, 2, \dots \text{ number of samples} \quad (4.1)$$

With this logic with simply two products (one with the signal shifted by 1 sample forward and one with the signal shifted by 1 sample backward) it was possible to extract all the indexes z corresponding to a zero-crossing. Notice that the signal is at the same time shifted also in its values, in such a way that a zero crossing corresponds to the exceeding of the threshold value.

At this point the number of elements to deal with has been drastically reduced and further

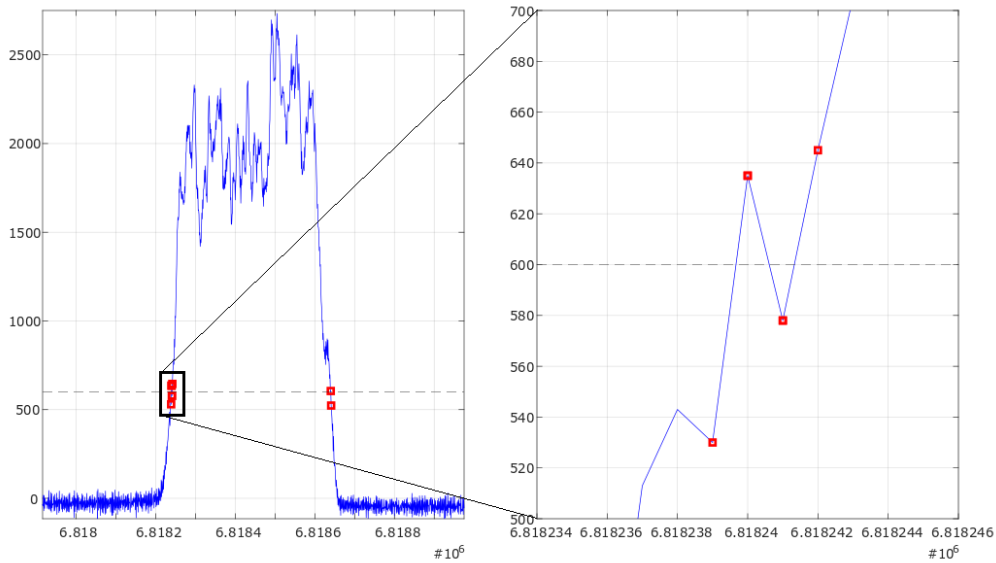


Figure 4.18: Points extracted from raw data after the first step

computations are more efficient.

However, as depicted in figure 4.18, the noise present in the signal has two principal effects:

1. More than two samples are detected for each threshold crossing

2. It's not possible to distinguish accurately between rising and falling edge

In order to solve these issues at this point it was needed to implement the hysteretic behaviour already discussed.

Speaking in terms of samples, in the case of the OPR signal it is easy to understand that the number of samples which represent the notch is smaller than the number of samples related to the rest of the surface, but it's bigger than the number of samples needed to detect the two edges of the notch. This considerations are always valid for each value of speed, because they depend on simple geometrical observations.

The hysteretic behaviour was obtained by considering the maximum speed, because in such a condition the number of samples recorded in each round is minimum. The set hysteresis value corresponds to the number of samples that the code has to 'wait' before being able to record another threshold crossing, and it was chosen a value slightly lower than the number of samples of a notch (for the OPR sensor) or blade (for the optical sensor) passage.

After this step the number of points was further reduced and corresponded to twice the number of blade crossings (because we have one point on the rising edge and another on the falling edge).

It was then necessary to choose if we want to consider the rising or falling edge as TOA indicator. Sometimes this choice can affect the measurements, but in this case the quality of rising and falling edge was the same both for the blades and for the notch. It was chosen the rising edge for detecting the blades and the falling edge for detecting the notch, without a particular reason.

After the implementation of proper values of hysteresis the situation was as depicted in figure 4.19, where is shown the same part of the signal seen in figure 4.18 for comparison.

After this procedure it was necessary to exclude from the vector the points related to incomplete rounds, so that at the end the number of points related to blades' pass was an integer multiple of the number of complete rounds.

It is evident that at this point there is one value of time for each blade passage and for each round, and we may use them in order to compute the blade tip displacements.

However it should be noted that there are two problems with the current TOA values, that depend on the noise:

1. The current TOAs don't correspond to a signal value equal to the set threshold. In fact at each TOA the signal assumes a different value which is slightly lower than the threshold
2. The spatial noise introduces a random distribution also in the TOAs, that therefore may lead to wrong computation of displacements

In order to reduce these undesired effects it has been introduced a linear regression method that is explained in the following paragraph.

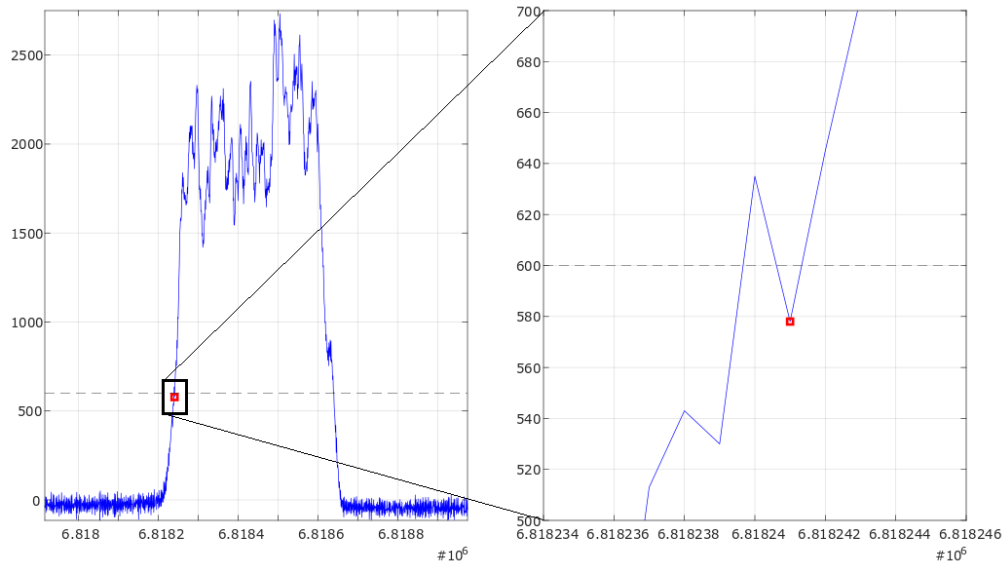


Figure 4.19: Points extracted from raw data after the implementation of hysteresis

Least squares linear regression for TOA approximation

Up to this point it was possible to detect one TOA value for each rising edge (for blades) and falling edge (for OPR). These points have not been used directly for the evaluation of displacements, but as a reference for computing a least squares linear regression.

In order to do that it was chosen to extract from the signal a certain number of points before and after the ones already available, in such a way that they would be representative of the signal values nearby the threshold chosen for triggering.

The amount of points has been chosen considering the maximum speed of the rotor, because in that case there are less values nearby the threshold.

Knowing the time values and the corresponding voltage levels it was possible for each signal edge to compute a line, obtaining the slope and the intercept by means of fast matrix operations executed with MatLab.

Once the lines were known, it was possible to compute the TOAs by finding the intersections between the lines and the threshold.

In figure 4.20 it is depicted a portion of the signal coming from a blade pass, showing the advantages of a linear regression. In fact we can see that all the new TOAs correspond to a signal value equal to the threshold and that the position of each point is approximately in the middle of all the threshold crossings due to noise.

The latter feature implies a reduction of the scattering caused by a random spatial noise distribution.

A portion of the MatLab code employed can be found in Appendix A.

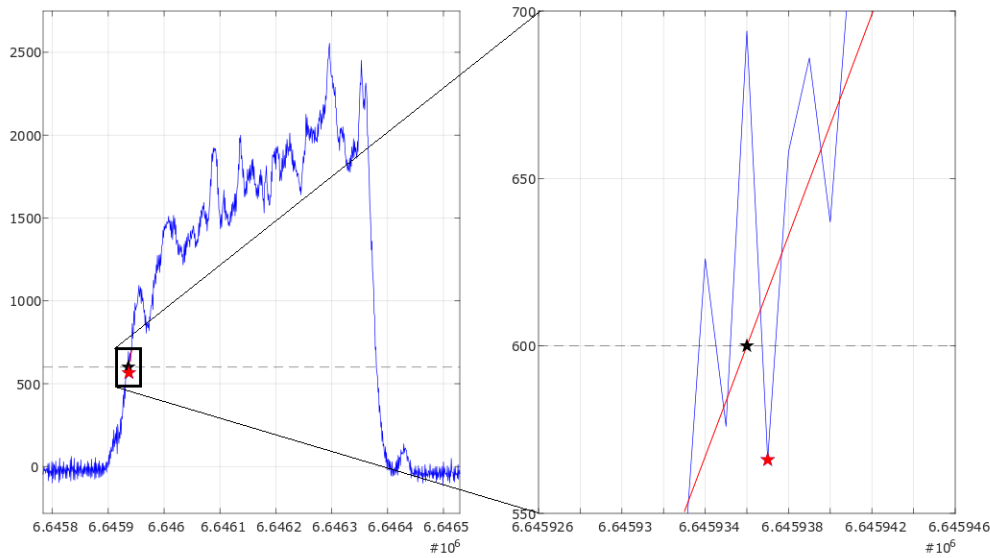


Figure 4.20: The black mark corresponds to the point used for TOA after that the linear regression has been performed. The red mark is the point considered before the linear regression.

4.3.2 One optical sensor configuration

Instruments

Digital acquisition devices

For measuring the TOA of blades it is necessary to use at least one analog sensor and a device which is able to convert its analog output in a digital one, in order to save the signal in the computer.

For what concerns the analog-to-digital device, it was employed a NI-9222 module plugged into a NI-cDAQ-9174 (Ethernet CompactDAQ Chassis with 8 slots) (figure 4.21). This module allows the simultaneous acquisition of 4 differential channels, with a maximum sampling rate of 500 kHz.

In figure 4.22 is shown the plot of a time limited portion of the signals coming from the blades and from the notch on the rotor at maximum speed, which shows that the sampling rate chosen was high enough to catch all the blades even when the sensor was positioned near the trailing edge, which is thinner than the leading edge and thus its passage in front of the sensor is faster and more difficult to detect.



Figure 4.21: Analog-to-digital acquisition device

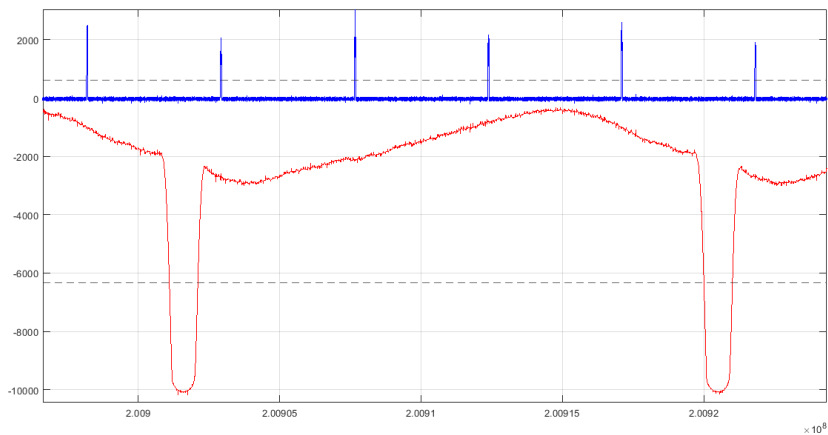


Figure 4.22: Portion of the signal coming from the trailing edge and the opr sensor at maximum speed

Eddy current sensor

Being the rotor made of conductive material, it was possible to think about the employment of an eddy current sensor for the acquisition of a one per revolution signal that would be used as a reference for the computation of blades' displacements and of the rotational speed of the assembly.

Two tasks had to be accomplished for that:

1. Finding a way to install the sensor in a position that allowed the detection of the

rotor, without influencing the air flow

2. Making a surface mark that could be used as a neat one per revolution reference

The first task was accomplished by exploiting the geometry of the engine. Luckily there were four holes on the surface of the engine which faced directly the bladed disk. Furthermore, the axial distance between this hole and the aluminium rotating disk was bigger enough for the sensor to be positioned there without interfering with the air flow.

From this observations it was designed a small bracket that could be fixed in some way to the engine cavity. The bracket has two holes, one threaded for fixing the sensor and one smooth for screwing it on the engine. The hole located on the engine surface had to be threaded in the ITWL workshop in order to be used for fixing the bracket.

For what concerns the second task, it was accomplished by simply cutting away a 2 mm layer of material from the surface of the rotor that would be detected by the sensor.

In figure 4.23 (b) is possible to view the opr sensor mounted on the engine and also the notch that was used as reference.

The distance between the sensor and the rotor surface was not constant because of tol-

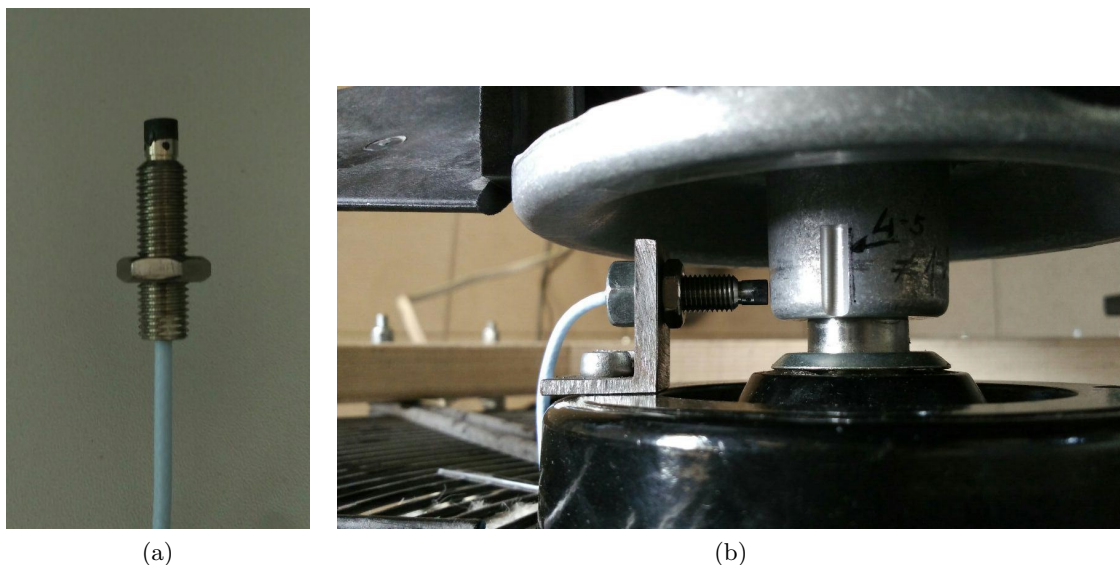


Figure 4.23: (a) Eddy current sensor, (b) Configuration for the OPR signal acquisition

erances, so the signal obtained without the notch is variable as well and has a sinusoidal shape. Anyway this was not a problem because the notch was neat and deep enough to allow a secure reference that could not be mistaken for this normal variation of the signal. In figure 4.24 is shown that the notch signal has an amplitude much bigger than the slight variation of the distance from the sensor.

During the first measurement attempt it was noticed a problem with the amplitude of the

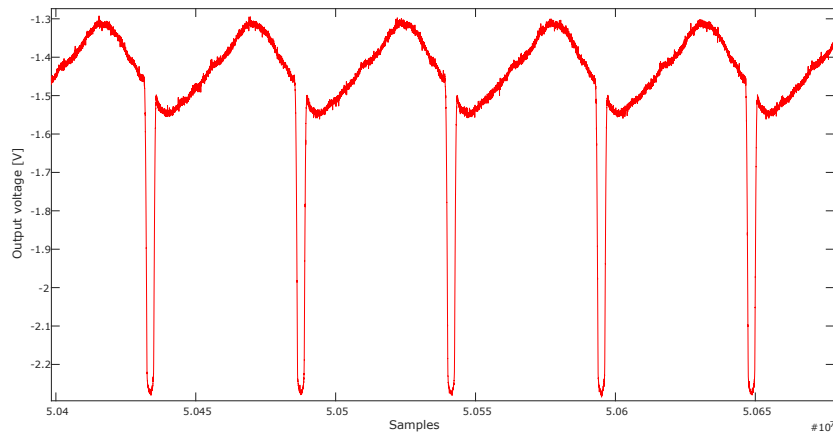


Figure 4.24: Sample of the OPR signal coming from the eddy current sensor

output voltage coming from the eddy current sensor. The module used for the acquisition allows a limited input voltage range, so if the amplitude of the analog signal exceeds this limit the output will be clipped at the maximum (or minimum value).

In this case the amplitude of the opr sensor was indeed too big and it was necessary to create a simple voltage divider in order to reduce it. In a first attempt it was employed a divider made with two equal resistances, which would provide a halving of the original output signal, as depicted in the scheme of figure 4.25.

Two resistances of $10\text{ k}\Omega$ each were used, this configuration came out to be good enough and no further modifications had to be made from this point of view.

There were some issues due to the fact that two different types of sensors were used for the detection of blades and notch. In applications that require high reliability it's preferable to use only one type of sensor for measuring both the displacements of blade tips and the rotor speed. In particular in figure 4.26 it is visible that the OPR signal is affected by a certain noise which we weren't able to eliminate.

In order to reduce the effect of this noise on the evaluation of opr TOAs it was undertaken a method explained in section 4.3.1. It was used also for a better extraction of blades' TOAs, even though the signal coming from the blade was affected by a different type of noise.

Optical sensor

As already described, the material of the blades is not ferromagnetic, so for the first measurements it was used an optical sensor. Unluckily there was only one available and so each blade could be detected only once per revolution.

The configuration used has one optical fiber in the middle as transmitter and six optical

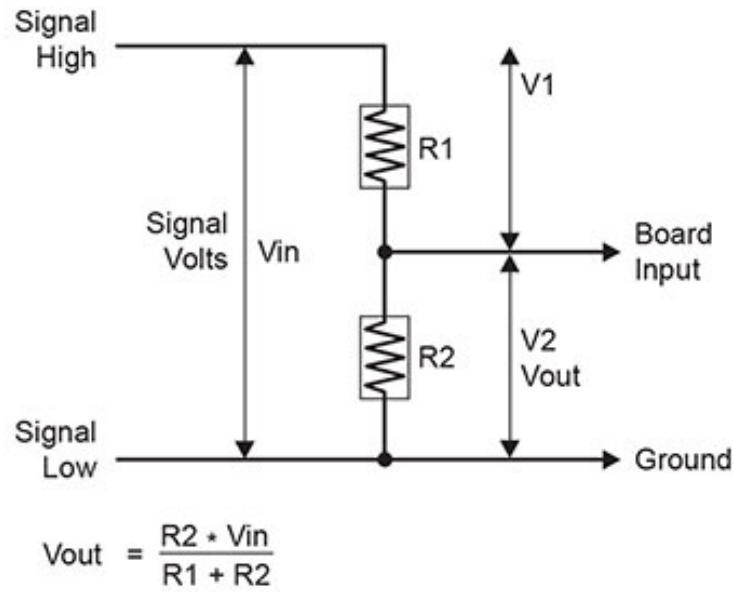


Figure 4.25: Electrical scheme of a generic voltage divider

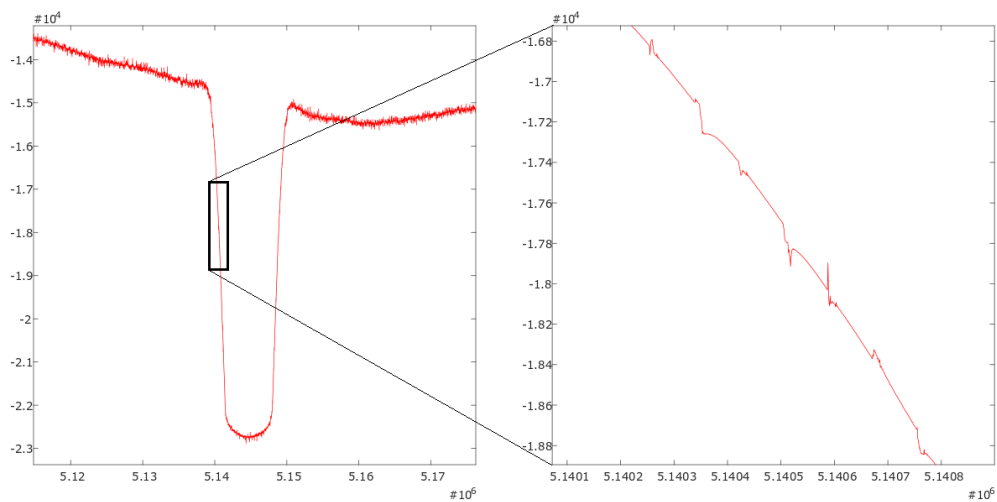


Figure 4.26: Detail showing the noise present in the OPR signal

fibers around as receiver.

The employment of a single fiber as transmitter implies that the signal slope is high, because it takes a very short time for the blade tip to block all the light emitted. This means that the spatial noise is reduced with respect to other configurations.

The blades have large tolerance because of their manufacturing process, so the clearance between them and the sensor was not constant. As an evidence in figure 4.27 it is possible to see a sort of amplitude pattern that repeats every four blade passages, and in section 3.6

it is explained that this phenomenon is due to the clearance differences.

In section 3.5.2 it was also discussed the issue of waveform quality in the case of optical

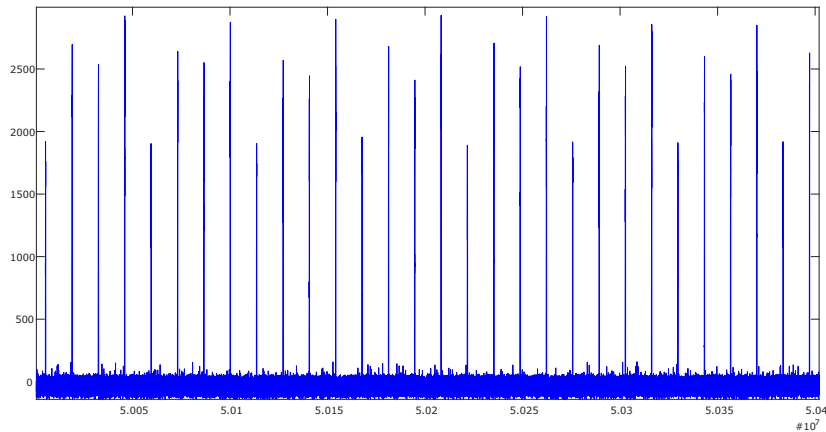


Figure 4.27: Optical signal related to blades, each vertical line corresponds to the detection of a blade

sensors, arriving to the conclusion that in order to perform a proper triggering with optical devices it would be better to have a clean target surface.

For this purpose the blade tips were polished before the measurements, so that the extraction of TOAs would be easier and above all more precise. In figure 4.28 it is shown a detail on the signal related to the same blade at low (a) and high (b) speed.

In this figure the vertical scale has been kept the same, in order to confirm that optical signal amplitude is not sensitive to the speed of blade tips.

There was the necessity to design a support, similarly to what was made with the opr sensor. In this case the situation was better because the space available was much more, in fact the sensor could be installed at different angular positions on the panel.

For what concerns the axial position it was chosen to make two holes in the support, one centered toward the leading edge and one on the trailing edge. In this way it was possible to compare the measurements and eventually distinguish between synchronous excitations related to the 2nd and 3rd mode shapes.

The reasoning was that, for instance, if at a certain rotational speed there would be a synchronous response on the trailing edge and not on the leading edge, the mode shape and the oscillation frequency involved were related to the 3rd mode.

In figure 4.29 there are two pictures that show the axial position of the sensor with respect to the blade tip.

Of course it was necessary to use a laser generator (figure 4.30), that was controlled by a suited software. This device allows the transmission and reception of a laser beam through

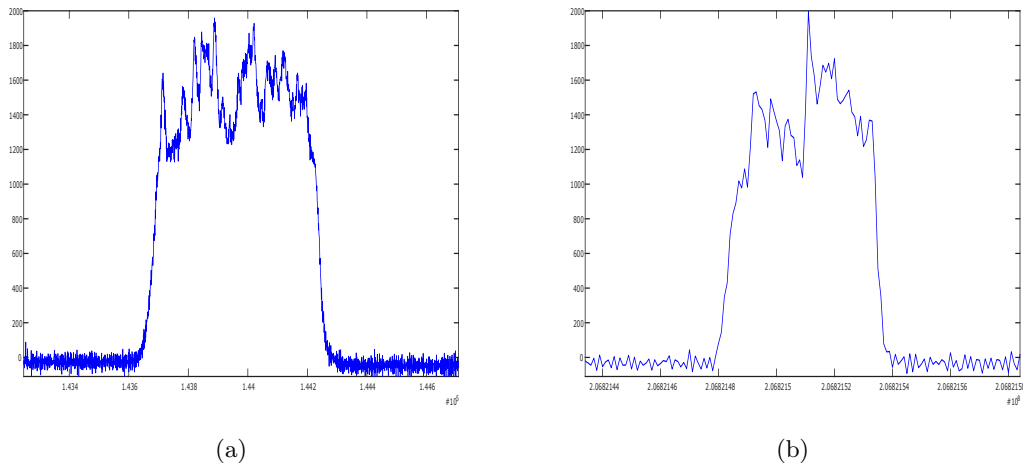


Figure 4.28: Detail on optical signal, the difference between the number of samples required for detecting the same blade at different speeds is evident.

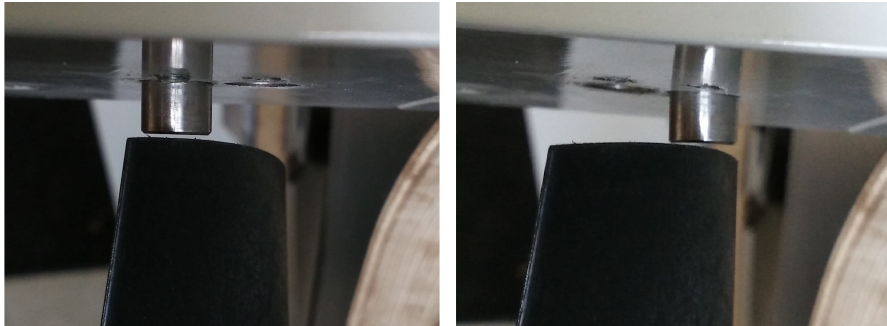


Figure 4.29: Axial positions of optical sensor

optical fibers, so its output is the detector signal proportional to the light coming from the sensor itself, that was connected to the cDAQ acquisition device.

The cables containing the optical fibers are delicate, and they had to be fixed properly in order to avoid problems due to the strong air flow during the tests.

Results

Tip deflection plots

As already described in section 3, the tip displacement can be computed multiplying the tip radius by the time difference between the TOA and a constant reference, which is the expected TOA of the blade.

These values were computed exploiting the notch on the rotor and assuming that the speed remains constant during a complete revolution.

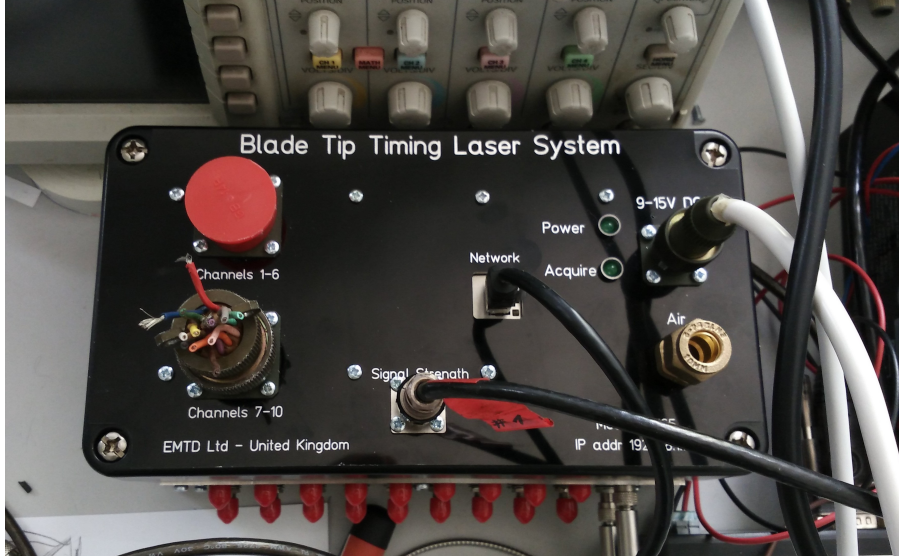


Figure 4.30: Laser generator employed for the measurements with optical sensor

The procedure consists in computing the average angular position over the whole test, calculated for each revolution as the speed multiplied by the difference between the TOA of the blade and the TOA of the notch:

$$\Theta_0 = \frac{1}{N} \sum_{i=1}^N \omega_i (TOA_{blade,i} - TOA_{notch,i}) \quad i = 1 \div N \quad (4.2)$$

Where N is the number of complete revolutions during a test.

Once the reference angle is known, the tip displacement vector can be computed as follows:

$$x_{ij} = r \cdot (\omega_i (TOA_{blade,ij} - TOA_{notch,i}) - \Theta_{0,j}) \quad j = 1 \div \text{number of blades} \quad (4.3)$$

Figure 4.31 shows a plot of the tip displacements for the different blades, with an offset of 0.01 mm between two consecutive blades for clarity. In this type of measurements, it is necessary to distinguish static and dynamic displacements, because they contribute differently to the stress state of the object of study and that's extremely important for the assessment of fatigue issues.

In order to extract the static components it was used the Savitzky-Golay filter, which executes a smoothing of the data by means of a low degree polynomial fitting, performed by the method of linear least squares.

The static displacements and the dynamic displacements are plotted in figures 4.32 and 4.33 respectively.

The former can be used in order to detect any synchronous vibrations using the Campbell

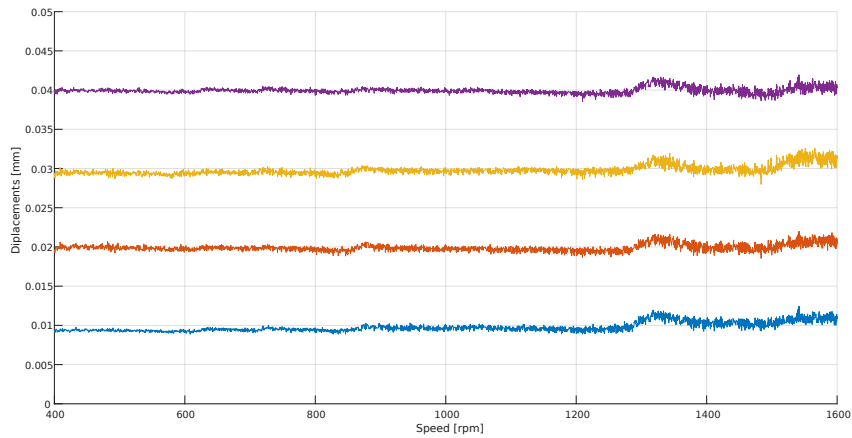


Figure 4.31: Tip displacements related to a test performed with increasing speed and optical sensor pointing near the trailing edge.

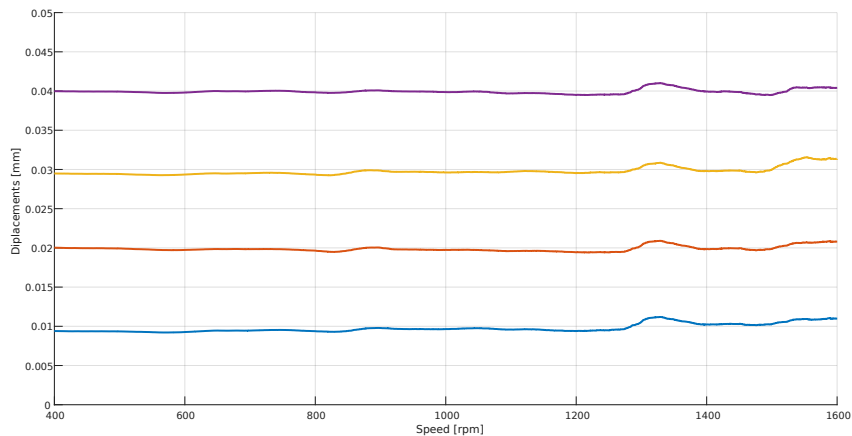


Figure 4.32: Low frequency tip displacements

diagram obtained from the FE model.

In this step it is important to be careful because it's not trivial to assert that a variation of the static displacement component is due to a synchronous vibration or not. In fact, as explained in section 3.4, there are many causes that can generate such type of tip displacements.

Moreover, the damping of the material has a heavy impact on the assessment of the displacement plots compared to the Campbell diagram, because two close resonances can be seen as one and thus the resulting considerations will be wrong.

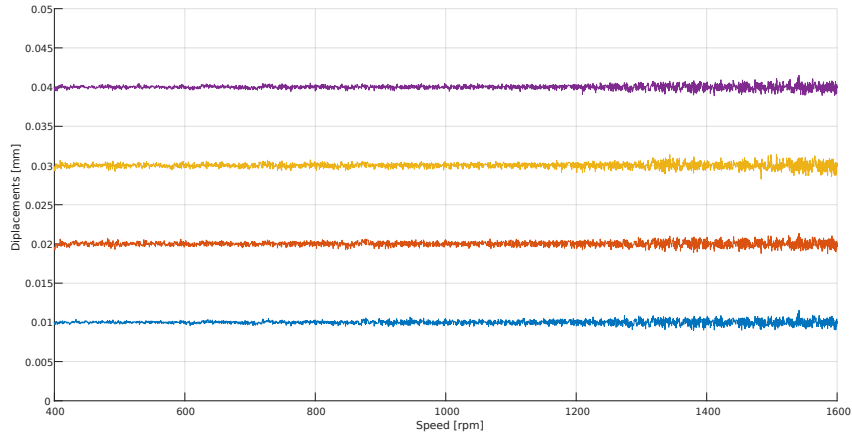


Figure 4.33: High frequency tip displacements

Single-blade spectrum

The spectrum analysis is needed in order to retrieve information about the blade vibrations, so it was necessary to use the displacements plotted in figure 4.33 in order to compute it properly.

One of the main assumptions related to the evaluation of a spectrum is that the sampling frequency of the signal must be constant, however in this case that is not true because of the nature of the measurement system. The sampling frequency of tip displacements is indeed proportional to the rotational speed.

With this consideration it becomes obvious that computing the FFT over the whole vector would be meaningless. Thus it was decided to perform the spectrogram of the signal using STFT (Short Time Fourier Transform), that is a Fourier-related transform used to determine the sinusoidal frequency and phase content of local sections of a signal as it changes over time.

In order to accomplish that it was exploited a MatLab function that allows the definition of the window size, type and overlap. The sampling frequency was set constant only temporarily, considering that the acceleration was not too high.

If we want the real oscillation frequency to be read on the y axis of the spectrogram, it has to be manipulated in such a way that it assumes the shape of a trapeze.

It was convenient to plot the Engine Order instead of the frequency, in this case the spectrogram remains rectangular and the EO of a certain resonance is referred to the corresponding speed on the x axis.

For this case it came out that a single blade spectrum is not enough for the characterization of vibrations, so for a better analysis the focus was moved on the all-blade spectrum.

All-blade spectrum

The all-blade analysis considers the bladed disk as a unified vibrating assembly and assumes the assembly vibrates in nodal diameter modes.

Since the signal is heavily undersampled and the angular speed is not very high, the response of the blades is not much evident from the first spectrogram (figure 4.34 (a)), moreover there were some unexpected peaks at high frequency and low frequency probably due to the phenomenon of leakage which had to be filtered.

In order to highlight the resonances the values of the spectrogram were clipped at a certain level, and the result is depicted in figure 4.34 (b).

In this figure is possible to visualize some resonances and the respective reflections, due

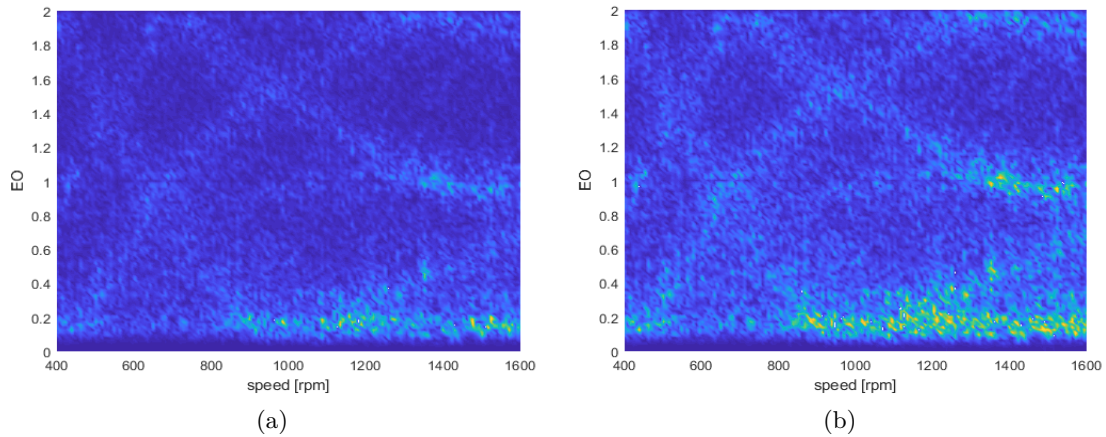


Figure 4.34: All-blade spectrogram obtained with data from the optical sensor

to the fact that the signal is undersampled and thus subjected to aliasing.

Moreover for the same reason the frequency resolution is pretty rough. Different window sizes and overlapping percentages were tested, but the best combination was the one depicted.

4.3.3 Six inductive sensors configuration

Instruments

The blades that are studied in this work are made of plastic and therefore it is not possible to directly use inductive sensors to detect their tip displacements, however it was possible to use a magnetic paint which was available after the measurement with optical sensors was completed.

A few layers of this paint on the blade tips made them detectable by inductive sensors. It was chosen to use 6 probes for the purpose.

For the OPR signal a new bracket was designed to fix the optical sensor (used previously to detect blades) to the motor, in the same way as was done for the eddy current probe. In figure 4.35 there's a picture of the assembly without rotor and blades in order to show the positions of the 6 inductive sensors and also of the optical one. In the next paragraph

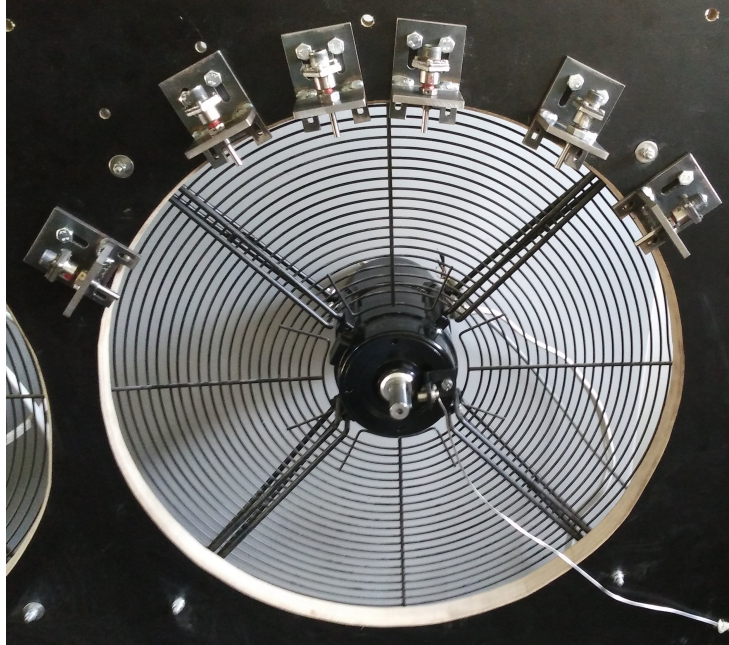


Figure 4.35: Picture of the second configuration of probes

more details are explained concerning the position of the probes, which is not random but follows a certain criterion.

For what concerns the acquisition system, it had to be changed too, since the number of channels required increased from 2 to 7.

This time it was necessary to use amplifiers in order to increase the output voltage of the inductive sensors, because the layer of magnetic paint was too thin to produce a signal with a high SNR.

The amplifiers, designed in ITWL, are prototypes, moreover their gain factor can be set by means of a suited LabView VI. Each amplifier has only two channels available, so 4 of them were needed.

The amplification factor was chosen considering the lowest speed, so that the SNR would be high enough for a correct operation of the triggering process. At low speed in fact the output voltage of magnetic pickups is minimum, as already explained in section 3.5.

The output of the amplifiers was connected to an analog-to-digital converter NI PXIe-6358 produced by National Instruments, which supports many input channels with a sampling frequency of 500 kHz each.

The computer employed for the signals' acquisition was a PXIe-8840 Quad-Core, also produced by National Instruments.

In this case too there was the same type of noise present in the previous tests. With proper grounding of the amplifiers and the inverter it was possible to get an acceptable output with relatively low noise.

Position of the frame

For this test the frame with the rotor and sensors assembled was mounted in the wind tunnel where it was designed to work in. Two further configurations were considered:

- Without obstacles (figure 4.36 (a))
- With one obstacle to excite synchronous vibrations (figure 4.36 (b))

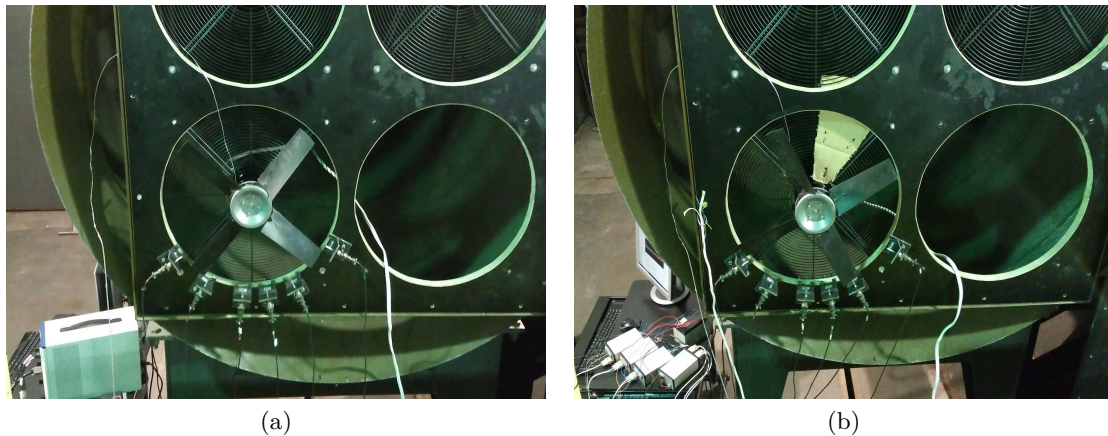


Figure 4.36: Frame installed on the wind tunnel, (a) with free flow and (b) with one obstacle

Probe positions

As already explained in section 3.5.3 the positions of probes around the casing/frame is crucial to the analysis of BTT data. The idea was to exploit a sine fitting algorithm in order to extract the frequency and amplitude data, so it was possible to choose a non-uniform spacing between the probes.

This choice was made because in case of uniform spacing the system is 'blind' to some engine orders. In fact if for example there is an equal spacing of 45° the system will be blind to all the engine orders which are multiple of $360/45$.

However an uneven probe spacing is not suitable in case of autoregressive or Fourier based

techniques.

Pickering in his master thesis [32] lays the attention on the effect that the probe spacing has on the results. In fact the condition number of the matrix D_0 (equation 4.8), should be as close to 1 as possible in order to get the best least square approximation. Using a software developed by the same company (EMTD Ltd.) which produces the laser generator in figure 4.30, it was possible to define a spacing which minimizes the condition number of D_0 , obtaining the following angles for the probes:

$$\theta_1 = 0^\circ \quad \theta_2 = 24^\circ \quad \theta_3 = 47^\circ \quad \theta_4 = 63^\circ \quad \theta_5 = 81^\circ \quad \theta_6 = 113^\circ \quad (4.4)$$

This set of angles is not the only one generated by the software, because it employs a Monte Carlo method and the problem is non linear, so every time it runs there is a different set as output. The angles in 4.4 are in fact the average of a few attempts.

However, the real probe positions do not coincide with the ones in 4.4 because of errors during the installation procedure. Exploiting the signal coming from the blades at constant speed it comes out that the real positions are:

$$\theta_1 = 0^\circ \quad \theta_2 = 22,73^\circ \quad \theta_3 = 47,23^\circ \quad \theta_4 = 62,76^\circ \quad \theta_5 = 80,75^\circ \quad \theta_6 = 113,77^\circ \quad (4.5)$$

Since the difference between the two sets is very small, the variation of the condition number was negligible and the positions were acceptable.

Non linear least squares sine fitting

Before the installation of sensors it was necessary to define the type of analysis that would have been used, which is non linear least squares sine fitting.

The algorithm is described in detail in [19], [20] and [33], its main assumption is that the tip displacement of each blade is modeled as a sum of sinewaves. In this way it can be expressed as follows:

$$x[n] = A_0 \cdot \cos(2 \cdot \pi \cdot EO \cdot \Omega \cdot t_n) + B_0 \cdot \sin(2 \cdot \pi \cdot EO \cdot \Omega \cdot t_n) + C_0 \quad (4.6)$$

Where Ω is the angular speed, EO is the known (if three-parameter fitting) or unknown (if four-parameter fitting) engine order of the vibration and A_0 , B_0 , and C_0 are the unknowns that minimize the following sum:

$$\sum_{n=1}^M [x[n] - A_0 \cdot \cos(2 \cdot \pi \cdot EO \cdot \Omega \cdot t_n) - B_0 \cdot \sin(2 \cdot \pi \cdot EO \cdot \Omega \cdot t_n) - C_0]^2 \quad (4.7)$$

Where M is the number of samples.

To find the values for A_0 , B_0 , and C_0 it is necessary to create the matrices D_0 and x :

$$D_0 = \begin{bmatrix} 1 & \sin(EO\theta_1) & \cos(EO\theta_1) \\ 1 & \sin(EO\theta_2) & \cos(EO\theta_2) \\ \dots & \dots & \dots \\ 1 & \sin(EO\theta_N) & \cos(EO\theta_N) \end{bmatrix} \quad x = \begin{bmatrix} x[1] \\ x[2] \\ \dots \\ x[M] \end{bmatrix} \quad (4.8)$$

Where θ_i is the fixed angular position of the probe i along the circumference and N is the number of probes.

In matrix notation, the sum of squared differences in equation 4.7 is given by

$$(x - D_0 s_0)^T (x - D_0 s_0) \quad (4.9)$$

where $s_0 = [A_0 \ B_0 \ C_0]^T$.

The least squares solution \hat{s}_0 that minimizes equation 4.9 is given by

$$\hat{s}_0 = (D_0^T D_0)^{-1} (D_0^T x) \quad (4.10)$$

Results

Tip deflection plots

The procedure followed in order to obtain the TOA and then the tip displacements was the same already explained in sections 4.3.1 and 4.3.2.

Considering only the tip displacements measured from the timing data of one sensor (figure 4.37), it is possible to notice that there is a big difference between the configuration without obstacle and the one with an obstacle on the dynamics of blades.

The reason is that an obstacle the airflow excites not only EO 1, but all the engine orders, even though with decreasing influence as the EO considered increases.

At first glance is evident that in both cases there is an overall static displacement component which increases linearly with the speed. It is likely due to the untwist or lean motion of blades.

Most importantly in the second configuration appear some localized static displacements at approximately 730 rpm, 860 rpm and 1300 rpm, which suggest that synchronous vibrations occur at those speeds.

Considering also the data from other sensors and low-pass filtering the displacements (figure 4.38) there is further confirmation, since the static displacements of the same blade have different values at different angular positions, as predicted by Heath [12] and shown theoretically in figure 3.5 for what concerns the speed range close to 730 rpm.

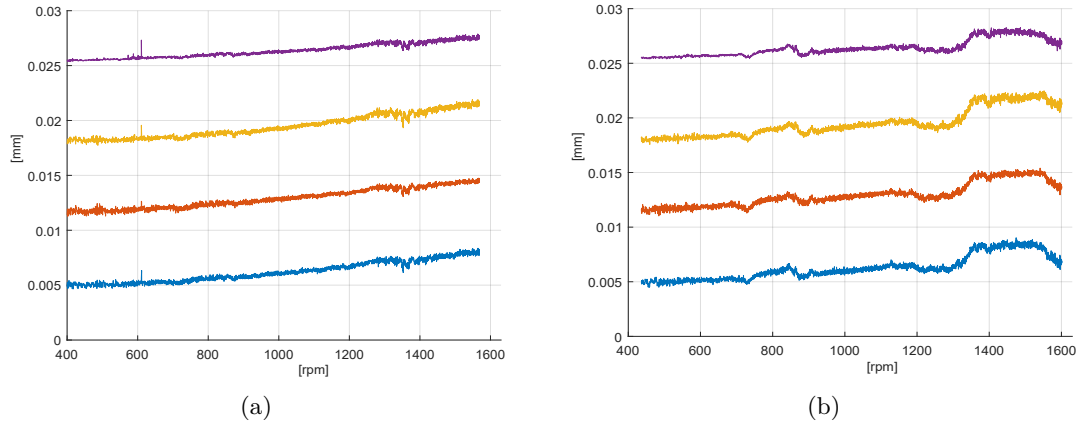


Figure 4.37: Tip displacements measured by sensor 5 during acceleration test, (a) with free flow and (b) with one obstacle

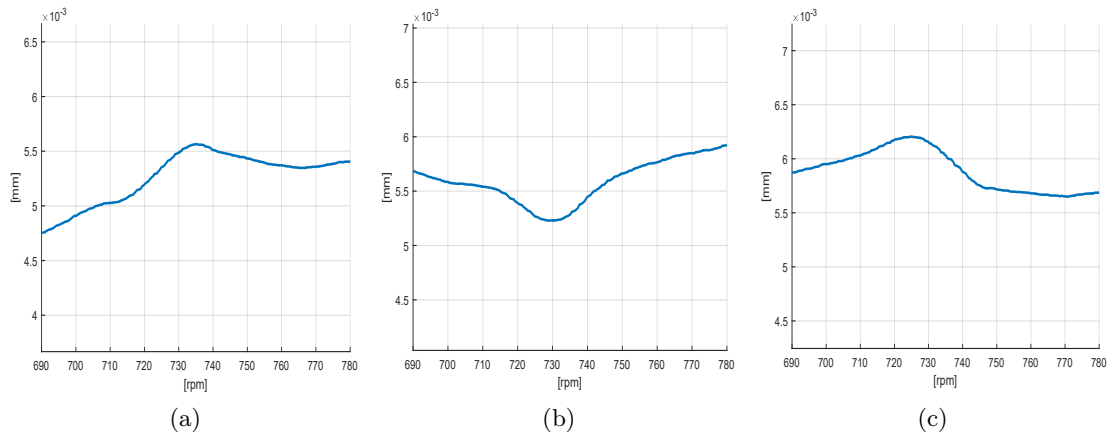


Figure 4.38: Details of static tip displacements measured by, (a) sensor 1 (b) sensor 2 and (c) sensor 3

All-blade spectrogram

As previously done in the configuration with one optical sensor, the spectrogram was plotted also in the case with six sensors.

Since the algorithm requires a uniform sampling, it was not possible to use simultaneously the signal from all the sensors as their spacing was not uniform.

The plot in figure 4.39 (a) is related to the signal coming from one sensor (number 6) before the clipping procedure already explained, while in figure 4.39 (b) is plotted the

same spectrogram after removing the numerical issues which made the plot unclear. In the latter graph a few resonances are visible and more clear than in the spectrogram obtained from the test with the optical sensor. This is probably due to the better position of the frame which granted a more uniform airflow, together with the presence of the obstacle that generated a more regular excitation.

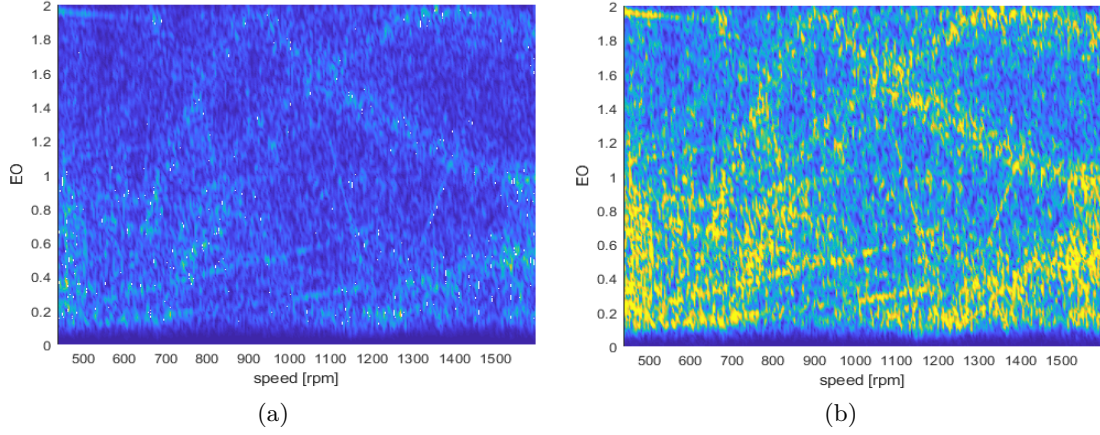


Figure 4.39: All-blade spectrogram obtained with data from inductive sensor number 6

Campbell plot

The least squares algorithm employed by the software to fit the BTT data gathered during the measurements lead to the results shown in tables 4.3, 4.4, 4.5, 4.6, 4.7 and 4.8.

blade	freq [Hz]	EO	rpm	A (pk-pk) [mm]	fit quality [%]
1	73.6	6	736	1.23	92
2	73.6	6	736	1.24	90
3	73.9	6	739	0.69	87
4	73.3	6	733	0.67	82

Table 4.3: M1E6 vibration parameters for all the blades

blade	freq [Hz]	EO	rpm	A (pk-pk) [mm]	fit quality [%]
1	71.2	5	854	1.17	95
2	70.9	5	850	1.77	98
3	71	5	851	1.48	98
4	70.6	5	848	1.65	97

Table 4.4: M1E5 vibration parameters for all the blades

blade	freq [Hz]	EO	rpm	A (pk-pk) [mm]	fit quality [%]
1	67.6	3	1351	3.52	98
2	67.7	3	1354	4	97
3	67.7	3	1354	2.68	97
4	67.6	3	1352	3.64	98

Table 4.5: M1E3 vibration parameters for all the blades

blade	freq [Hz]	EO	rpm	A (pk-pk) [mm]	fit quality [%]
1	268.4	12	1342	4.74	99
2	269.8	12	1349	6.51	98
3	270	12	1350	4.09	98
4	268.4	12	1342	5.1	99

Table 4.6: M1E3 vibration parameters for all the blades

blade	freq [Hz]	EO	rpm	A (pk-pk) [mm]	fit quality [%]
1	288.3	13	1331	3.86	98
2	288.3	13	1331	4.87	99
3	288.4	13	1331	3.12	98
4	287.7	13	1328	4.18	97

Table 4.7: M2E13 vibration parameters for all the blades

blade	freq [Hz]	EO	rpm	A (pk-pk) [mm]	fit quality [%]
1	319.7	15	1279	1.71	94
2	320.1	15	1281	2.3	97
3	319.9	15	1279	1.38	93
4	323.2	15	1293	1.53	92

Table 4.8: M3E15 vibration parameters for all the blades

Where A is the amplitude of tip oscillations.

Two main considerations can be made:

- In all the cases blade number 2 has the largest tip oscillation (Figure 4.40)
- Simultaneous synchronous vibrations occur in the speed range [1270÷1355 rpm]

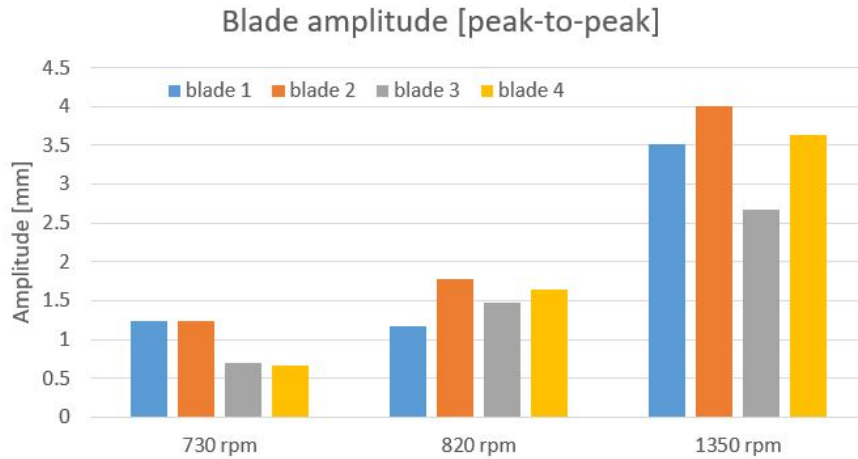


Figure 4.40: Amplitude of blade tip displacements for the synchronous vibrations involving the first mode shape

The issue with the vibration amplitude of blade 2 seems a problem, but it is not, because the oscillation frequency is always pretty much the same as the other blades, so the different amplitude is more likely to be due to a different inclination of the blade tip, caused by manufacturing tolerances.

For a better understanding of the situation these results are also synthesized graphically in figure 4.41, where is shown a comparison between the resonances expected by the model (green dots) and the resonances evaluated by the software (black dots) which are numerically expressed in the previous tables.

For clarity there are circles which surround points that should be coincident if the model was exactly representative of the real situation.

It is possible to notice that a good correspondence is obtained only for the vibrations involving the first mode, excited mostly by EO 3, 5 and 6. For these resonances it happens that the model underestimates slightly the oscillation frequency.

The reason of this issue lies on the modeling of the blade root, which in reality is not perfectly fixed. This problem requires further analysis that could not be made in the present work. For what concerns the other resonances involving modes 2 and 3, there is too much difference between the measurements and the model, with the latter overestimating the

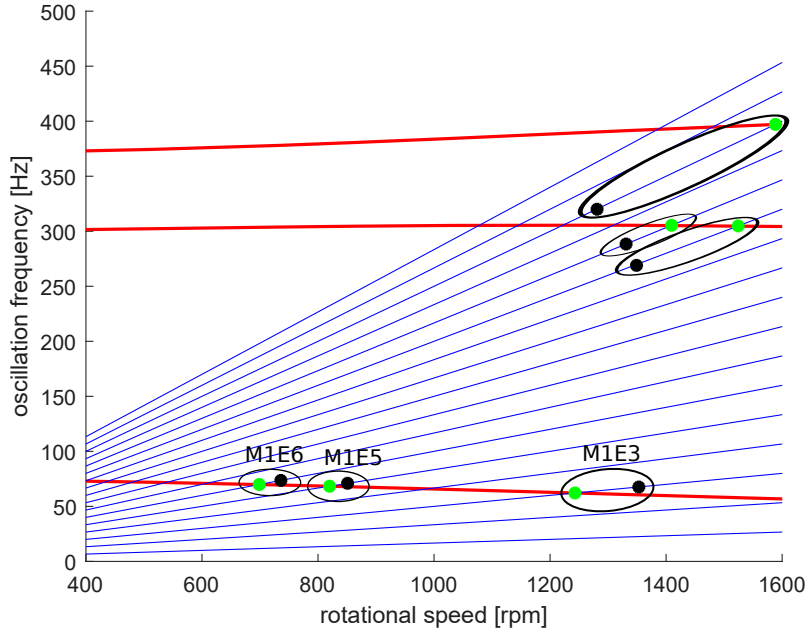


Figure 4.41: Campbell diagram with measured and predicted resonances

oscillation frequency in all the cases.

This is a consequence of the high uncertainty involving the modeling approximations about anisotropy and more details about this issue are explained in the next section.

4.4 Experimental validation of FEM model

Since the material properties of the blades such as elastic modulus, density and damping were known with too low precision, it was necessary to proceed with the experimental evaluation of the FRF of one blade in order to tune the parameters that had to be set as input in the FEM model.

4.4.1 Frequency response measurement

The experimental FRF was obtained through a hammer test, using a piezoelectric accelerometer located near the tip of the blade and a hammer with piezoelectric head used as impulse excitation and trigger (figure 4.42 (a) and (b)).

The blade was hanging from a support fixed with just a wire, so it could be considered free to vibrate in any direction with basically no constraints.

From a preliminary modal analysis computed using the FEM model of the undamped blade



Figure 4.42: (a) Accelerometer and (b) hammer used for the evaluation of the FRF of the blade

the first three natural frequencies were respectively 245, 446 and 634 Hz.

The sampling frequency was equal to 1638.4 Hz, so the maximum detectable vibration frequency was 819.2 Hz and then it was possible to detect the first three resonances, whose amplitude is plotted in figure 4.43.

The first three resonances (taking the frequency values where a peak occurs) actually

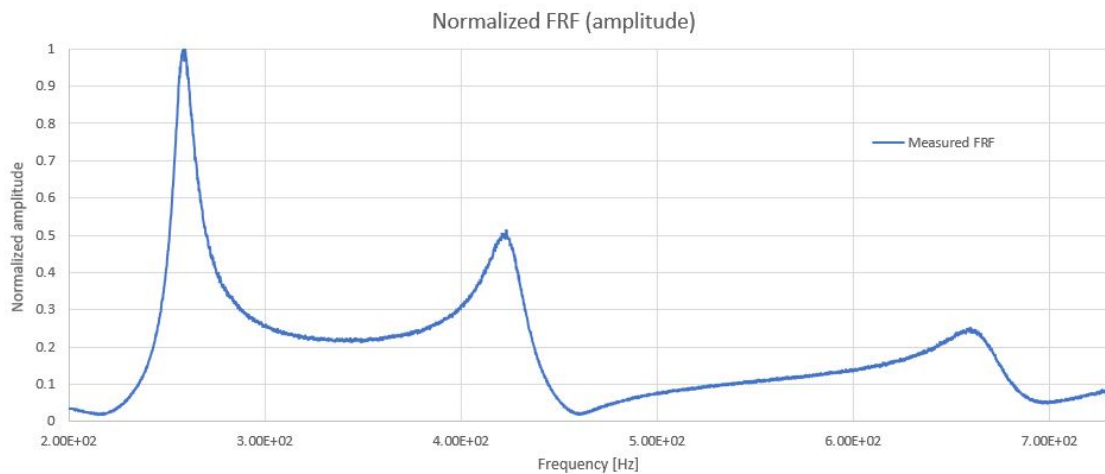


Figure 4.43: Frequency response (receptance) obtained with the hammer test

occurred at the frequencies 259 Hz, 423 Hz and 662 Hz respectively, so the the model needed some adjustments from the material point of view.

4.4.2 Damping and elastic modulus identification

The natural frequencies generically depend on the values of density, elastic modulus and less significantly on the damping of the material. The density was measured by simply dividing its weight by the volume computed by the CAD software, resulting in 1214.9 kg/m^3 . In this way it was considered a uniform density throughout all the blade volume, which is an approximation.

The following step was to identify the elastic modulus.

Elastic modulus

In a first attempt it has been used the Young's modulus declared by the manufacturer of the blade (6 GPa) as input in the FEM model. With this value the first natural frequency was equal to 248 Hz, thus too low with respect to the real one. After a few attempts it was found that in order to have correspondence between the measured and modeled FRF (considering only the first resonance) the correct values of Young's modulus for the blade's material is 6.64 GPa.

Using this value of elastic modulus there was an issue with the second resonance frequency, in fact from the model it came out a resonance at 469 Hz, about 46 Hz more than the real one (figure 4.46). The origin of this problem probably lies in the wrong assumption of isotropy of the material, both for what concerns the density and the elastic modulus.

This error brings the uncertainty in the evaluation of frequencies excited by higher engine orders, as explained previously.

Structural damping

Polymers have naturally the property to absorb vibrational energy better than metals due to their higher structural (or hysteretic) damping.

In literature there are some techniques to extract the damping of a component or a structure depending on the type of damping that it is subjected to. A component can be modeled by considering only viscous damping, only structural damping or both, anyway in this case only the hysteretic damping was taken into account.

For viscoelastic materials usually the damping is also depending on the vibration frequency, but in this case it was considered constant.

In order to find the constant structural damping coefficient η it was employed the Kennedy-Pancu method [34], whose working principle is briefly explained in the following.

In its basic configuration, the frequency response of a SDOF system with hysteretic damping is considered:

$$\frac{X}{f_0} = \frac{1}{k - m\Omega^2 + ik\eta} \quad (4.11)$$

Kennedy and Pancu observed that the expression 4.11 describes a circle with center $(0, -1/2k\eta)$ and radius $1/2k\eta$ in the Argand-Gauss plane (figure 4.44). By choosing two points **a**

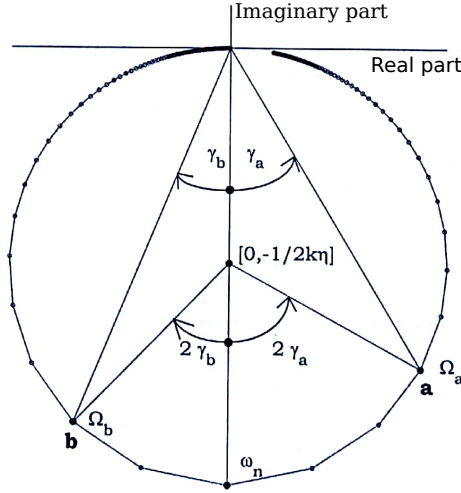


Figure 4.44: Nyquist circle for hysteretic damping

and **b** in such a way that $\Omega_a < \omega_n$ and $\Omega_b > \omega_n$, after some simple geometric considerations it comes out:

$$\eta = \frac{\Omega_b^2 - \Omega_a^2}{\omega_n^2 (\operatorname{tg}\gamma_a + \operatorname{tg}\gamma_b)} \quad (4.12)$$

Where η is the loss factor, or structural damping coefficient.

In practice the definition of the circle is not so straightforward as in theory, in fact there are a few complications to be dealing with:

- None of the experimental points lays on a perfect circle
- In the case of MDOF systems the circle moves in the plane and could be deformed

The first issue was taken into account by using 4 different combinations of angles γ_a and γ_b , so that it was possible to use the average value of damping. Furthermore in the case of MDOF systems there is a circle for each resonance (figure 4.45) and the damping factor was averaged also on the first three modes.

For the second issue, it has to be said that the deformations are not very big and can often be neglected. The centers of the circles were found also by averaging the real and imaginary parts of all the points.

Applying the Kennedy-Pancu method lead to a constant structural damping coefficient equal to 0.0438.

Figure 4.46 shows a comparison between the measured FRF and the FRF obtained from the FEM model updated with the new identified parameters. It is possible to notice that

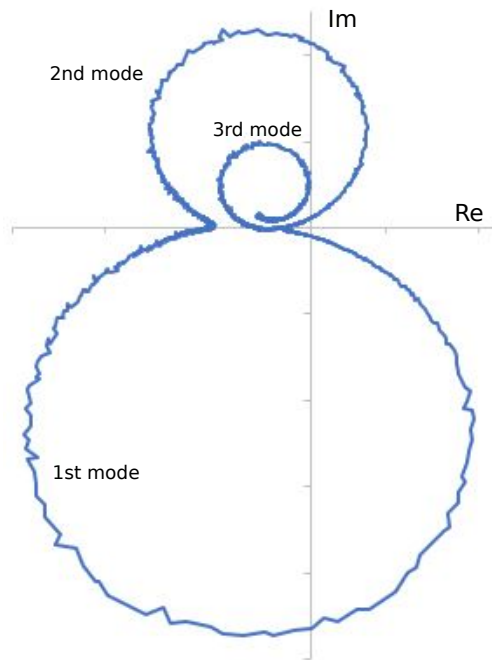


Figure 4.45: Experimental Nyquist circles of the first three resonances of the blade

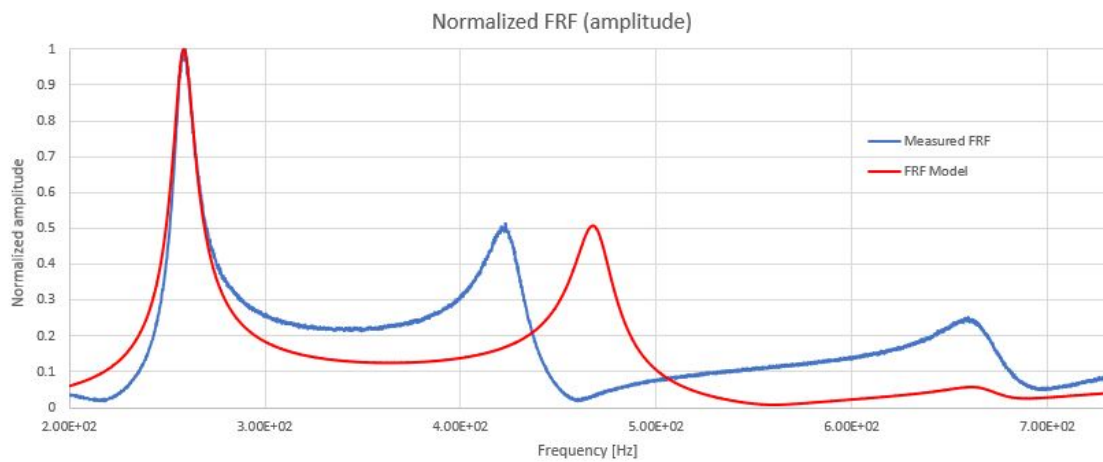


Figure 4.46: FRF (receptance) obtained with the hammer test and FRF computed with the model

there is a good correspondence with the first resonance, but the frequency at which occurs the second resonance is too different, as already mentioned previously.

For the third resonance there is apparently an issue with the amplitude, but this is not a real problem because it depends simply on the point where the force is applied in the model, and we are interested just in the frequency, which corresponds to the measured one.

Chapter 5

Conclusions

In this work the basic features of BTT method were successfully used to characterize the vibration of a plastic fan blade employed in a wind tunnel.

The technique was applied in two different configurations: using only one optical sensor and using six inductive sensors for the detection of the blades. Both the results gave similar outputs for what concerns the identification of the speed at which synchronous resonances occur.

Moreover in the latter case it was possible, by employing an appropriate algorithm, to evaluate more precisely the oscillation amplitude and frequency.

The signals transmitted by the sensors which detected the blades were manipulated by using a linear regression fitting in order to get rid of the noise generated by the instruments that could lead to mistiming issues.

A finite element model of the blade and the assembly was made, which lead to an output result that conforms to the frequency values obtained from the analysis of BTT measurements.

Further improvements could involve a better model which considers the friction at the blades' roots, because it influences the type of constraint and is an additional source of damping, so must be taken into account.

The model did not predict well the high frequency vibration modes of the blade. In order to improve this part it is needed a better knowledge of the anisotropy of the blade, both for what concerns its stiffness and its density.

These issues are relevant in this case because of the material (polypropylene glycole) and the process employed for the manufacturing of the blade, but for other applications the approximation of isotropic material usually works better.

Bibliography

- [1] V. Kharyton, *Faults Detection in Blades of an Aviation Engine in Operation*. PhD thesis, Ecole Centrale de Lyon, 2009.
- [2] R. Szczepanik, “Early Detection of Fatigue Cracks in Turbine Aero-Engine Rotor Blades During Flight,” *Journal of KONES. Powertrain and Transport*, vol. 20, no. 1, pp. 337–342, 2015.
- [3] R. Szczepanik, *Experimental Investigations of Aircraft Engine Rotor Blade Dynamics*. 2013.
- [4] R. Tomassini, “Blade Tip Timing and Blade Tip Clearance Measurement System Based on Magnetoresistive Sensors,” 2017.
- [5] O. Jousselin, *Development of Blade Tip Timing Techniques in Turbo Machinery*. PhD thesis, 2013.
- [6] B. K. Choi, “Pattern optimization of intentional blade mistuning for the reduction of the forced response using genetic algorithm,” *KSME International Journal*, vol. 17, no. 7, pp. 966–977, 2003.
- [7] Y. Kaneko, M. Ohta, K. Mori, and H. Ohyama, “Study on Vibration Response Reduction of Bladed Disk by Use of Asymmetric Vane Spacing : Effect of Asymmetric Vane Spacing on Response of Mistuned Bladed Disk,” *The Proceedings of the Dynamics & Design Conference*, vol. 2011, no. 0, pp. _533–1_–_533–12_, 2017.
- [8] P. Russhard, *Development of a blade tip timing based engine health monitoring system*. PhD thesis, School of Mechanical Aerospace and Civil Engineering, Manchester University, 2010.
- [9] NATO Science and Technology Organization, “Gas Turbine Engine Test Cell Instrumentation,” tech. rep., AVT-180, 2015.
- [10] P. E. McCarthy and J. W. Thompson, “Development of a Noninterference Technique for Measurement of Turbine Engine Compressor Blade Stress,” tech. rep., Arnold Engineering Development Center, 1980.
- [11] S. Heath, *A study of tip-timing measurement techniques for the determination of bladed-disk vibration characteristics*. PhD thesis, Imperial College London, 1997.

- [12] S. Heath and M. Imregun, “An improved single-parameter tip-timing method for turbomachinery blade vibration measurements using optical laser probes,” *International Journal of Mechanical Sciences*, vol. 38, no. 10, pp. 1047–1058, 1996.
- [13] S. Heath, “A New Technique for Identifying Synchronous Resonances Using Tip-Timing,” *Journal of Engineering for Gas Turbines and Power*, vol. 122, no. 2, p. 219, 2000.
- [14] G. Rigosi, G. Battiato, and T. M. Berruti, “Synchronous vibration parameters identification by tip timing measurements,” *Mechanics Research Communications*, vol. 79, pp. 7–14, 2017.
- [15] G. Rigosi, *Blade Tip Timing Technique : Theoretical Principles and Simulation of an Experimental Test*. PhD thesis, Politecnico di Torino, 2015.
- [16] I. Y. Zablotkiy and Y. A. Korostelev, “Measurement of Resonance Vibrations of Turbine Blades with the ELURA Device,” *Energomashinostroneniye*, 1970.
- [17] J. Gallego-Garrido, G. Dimitriadis, and J. R. Wright, “A Class of Methods for the Analysis of Blade Tip Timing Data from Bladed Assemblies Undergoing Simultaneous Resonances—Part I: Theoretical Development,” *International Journal of Rotating Machinery*, vol. 2007, pp. 1–11, 2007.
- [18] G. Dimitriadis, I. B. Carrington, J. R. Wright, and J. E. Cooper, “Blade-tip timing measurement of synchronous vibrations of rotating bladed assemblies,” *Mechanical Systems and Signal Processing*, vol. 16, no. 4, pp. 599–622, 2002.
- [19] IEEE, *IEEE Std 1057™-2007, IEEE Standard for Digitizing Waveform Recorders*, vol. 2007. 2007.
- [20] K. Kaźmierczak and R. Przysowa, “Standard sine fitting algorithms applied to blade tip timing data,” *Journal of Konbin*, vol. 30, no. 1, pp. 21–30, 2014.
- [21] A. P. Kurkov and H. S. Dhadwal, “Simultaneous Optical Measurements of Axial and Tangential Steady-State Blade Deflections,” no. March, p. V004T04A017, 2014.
- [22] M. Mohamed, P. Bonello, and P. Russhard, “A novel method for the determination of the change in blade tip timing probe sensing position due to steady movements,” *Mechanical Systems and Signal Processing*, vol. 126, pp. 686–710, 2019.
- [23] M. Eberlinc, M. Dular, B. Širok, and B. Lapanja, “Influence of blade deformation on integral characteristic of axial flow fan,” *Strojniski Vestnik/Journal of Mechanical Engineering*, vol. 54, no. 3, pp. 159–169, 2008.
- [24] D. H. Diamond, P. S. Heyns, and A. J. Oberholster, “Improved Blade Tip Timing measurements during transient conditions using a State Space Model,” *Mechanical Systems and Signal Processing*, vol. 122, pp. 555–579, 2019.
- [25] C. Liu and D. Jiang, “Improved blade tip timing in blade vibration monitoring with torsional vibration of the rotor,” *Journal of Physics: Conference Series*, vol. 364, no. 1, 2012.

- [26] J. Zhang, F. Duan, G. Niu, J. Jiang, and J. Li, “A blade tip timing method based on a microwave sensor,” *Sensors (Switzerland)*, vol. 17, no. 5, pp. 1–11, 2017.
- [27] International Society of Automation, “Tip Timing Waveform Quality (Draft ISA 107),” 2019.
- [28] E. O. Doebelin, *Measurement Systems: Application and Design*. McGraw-Hill, 5 ed., 2003.
- [29] Hood Technology Corp., “Hood Tech Optical Sensors Catalogue,” 2019.
- [30] I. García, J. Beloki, J. Zubia, G. Aldabaldetrekú, M. Asunción Illarramendi, and F. Jiménez, “An optical fiber bundle sensor for tip clearance and tip timing measurements in a turbine rig,” *Sensors (Switzerland)*, vol. 13, no. 6, pp. 7385–7398, 2013.
- [31] J. D. Denton, “Loss Mechanisms in Turbomachines,” p. V002T14A001, 2015.
- [32] T. M. Pickering, “Methods for Validation of a Turbomachinery Rotor Blade Tip Timing System Methods,” 2014.
- [33] R. Przynowa, “The analysis of synchronous blade vibration using linear sine fitting,” *Journal of Konbin*, vol. 30, no. 1, pp. 5–19, 2014.
- [34] A. Fasana and S. Marchesiello, *Meccanica delle vibrazioni*. Torino: CLUT, 2006.
- [35] D. J. Ewins, *Modal testing: Theory, practice and application*. Research studies press Ltd., second ed., 2000.
- [36] I. B. Carrington, J. R. Wright, J. E. Cooper, and G. Dimitriadis, “A comparison of blade tip timing data analysis methods,” *Proceedings of the Institution of Mechanical Engineers, Part G: Journal of Aerospace Engineering*, vol. 215, no. 5, pp. 301–312, 2001.
- [37] G. Battiato, C. M. Firrone, and T. M. Berruti, “A Benchmark for Tip Timing Measurement of Forced Response in Rotating Bladed Disks,” *Proceedings of the 11th International Conference on Engineering Vibration*, no. September, pp. 1–13, 2015.
- [38] J. S. Rao, *History of Rotating Machinery Dynamics*, vol. 20 of *History of Mechanism and Machine Science*. Dordrecht: Springer Netherlands, 2011.
- [39] B. D. Hockaday, “Comparing lensed and un-lensed optical spot probes for blade tip timing measurements,” pp. 1–9, 2012.
- [40] N. Jamia, M. I. Friswell, and S. El-Borgi, “The effect of sensor characteristics on blade tip timing measurements,” *Proceedings of the 11th International Conference on Vibrations in Rotating Machinery*, pp. 299–307, 2016.
- [41] C. Fan, P. Russhard, A. Wang, Y. Chen, and W. Dong, “Analysis of blade tip timing data from fan blades with synchronous and non-synchronous vibration,” *Journal of Physics: Conference Series*, vol. 1149, no. 1, 2018.
- [42] P. Tappert and D. Losh, “Analyze Blade Vibration 6 . 1 User Manual Prepared by : Hood Technology Corporation,” no. October, 2007.

- [43] R. Przysowa and E. Rokicki, “Inductive sensors for blade tip-timing in gas turbines,” *Journal of Konbin*, vol. 36, no. 1, pp. 147–164, 2015.
- [44] R. Przysowa and P. Russhard, “Non-contact measurement of blade vibration in an axial compressor,” *Proc IMechE Part C: J Mechanical Engineering Science*, 2019.
- [45] M. Witoś, “High Sensitive Methods for Health Monitoring of Compressor Blades and Fatigue Detection,” *The Scientific World Journal*, vol. 2013, no. May, pp. 1–31, 2013.
- [46] S. P. Zhu, P. Yue, Z. Y. Yu, and Q. Wang, “A combined high and low cycle fatigue model for life prediction of turbine blades,” *Materials*, vol. 10, no. 7, pp. 1–15, 2017.
- [47] P. Procházka and F. Vaněk, “Contactless diagnostics of turbine blade vibration and damage,” *Journal of Physics: Conference Series*, vol. 305, no. 1, 2011.
- [48] M. Witos and M. Wachlaczenko, “Structural Health Monitoring of Compressor Blades with the use of Variable Reluctance Sensor and Impedance Method,” *Proceedings of the 19th World Conference on Non-Destructive Testing*, no. June, pp. 1–8, 2016.

Appendix A

MatLab code

Here is shown the portion of the code developed in order to get the improved extraction of TOAs by means of linear regression.

```
1 %% Least-square linear interpolation
2
3 % interpolation of blades' signal
4 for n = 1:2*lim_s+1
5     if n == 1
6         LSt_s(n,:) = z_s-lim_s;
7     else
8         LSt_s(n,:) = LSt_s(1,:) + (n-1)*ones(1,length(z_s));
9     end
10 end
11 for m = 1:length(z_s)
12     for n = 1:2*lim_s+1
13         LSy_s(n,m) = sig(LSt_s(n,m)); % I put the corresponding values of the ...
            points in the matrix LSy
14     end
15 end
16
17 for h = 1:length(z_s)
18     X_s = [ones(2*lim_s+1,1) LSt_s(:,h)];
19     b_s(:,h) = pinv(X_s)*LSy_s(:,h);
20     %b_s(:,h) = X_s\LSy_s(:,h);
21 end
22 a_j_s = b_s(1,:);
23 b_j_s = b_s(2,:);
24
25 % Interpolation of opr signal
```

```
26 for n = 1:2*lim_o+1
27 if n == 1
28 LSt_o(n,:) = z_o-lim_o;
29 else
30 LSt_o(n,:) = LSt_o(1,:) + (n-1)*ones(1,length(z_o));
31 end
32 end
33 for m = 1:length(z_o)
34 for n = 1:2*lim_o+1
35 LSy_o(n,m) = opr(LSt_o(n,m)); % I put the corresponding values of the ...
    points in the matrix LSy
36 end
37 end
38 for h = 1:length(z_o)
39 X_o = [ones(2*lim_o+1,1) LSt_o(:,h)];
40 b_o(:,h) = pinv(X_o)*LSy_o(:,h);
41 %b_o(:,h) = X_o\LSy_o(:,h);
42 end
43 a_j_o = b_o(1,:);
44 b_j_o = b_o(2,:);
45
46 %% TOA from interpolation
47
48 TOA_s_index = (thresh-a_j_s)./b_j_s + start;
49 TOA_s = TOA_s_index*dt;
50
51 TOA_o_index = (thresh_opr-a_j_o)./b_j_o + start;
52 TOA_o = TOA_o_index*dt;
```